Journal of Computational Physics 448 (2022) 110752

Contents lists available at ScienceDirect

Journal of Computational Physics

www.elsevier.com/locate/jcp

A fully decoupled linearized finite element method with second-order temporal accuracy and unconditional energy stability for incompressible MHD equations

Guo-Dong Zhang [a], Xiaoming He [b], Xiaofeng Yang [c,*]

[a] *School of Mathematics and Information Sciences, Yantai University, Yantai, 264005, Shandong, PR China*
[b] *Department of Mathematics and Statistics, Missouri University of Science and Technology, Rolla, MO, 65409, USA*
[c] *Department of Mathematics, University of South Carolina, Columbia, SC, 29208, USA*

ARTICLE INFO

Article history:
Available online 11 October 2021

Keywords:
MHD
Finite element method
Second-order
Fully-decoupled
Unconditional energy stability
Linearized

ABSTRACT

For highly coupled nonlinear incompressible magnetohydrodynamic (MHD) system, a well-known numerical challenge is how to establish an unconditionally energy stable linearized numerical scheme which also has a fully decoupled structure and second-order time accuracy. This paper simultaneously reaches all of these requirements for the first time by developing an effective numerical scheme, which combines a novel decoupling technique based on the "zero-energy-contribution" feature satisfied by the coupled nonlinear terms, the second-order projection method for dealing with the fluid momentum equations, and a finite element method for spatial discretization. The implementation of the scheme is very efficient, because only a few independent linear elliptic equations with constant coefficients need to be solved by the finite element method at each time step. The unconditional energy stability and well-posedness of the scheme are proved. Various 2D and 3D numerical simulations are carried out to illustrate the developed scheme, including convergence/stability tests and some benchmark MHD problems, such as the hydromagnetic Kelvin-Helmholtz instability, and driven cavity problems.

1. Introduction

When a conductive fluid moves in an electromagnetic field, an electric current is generated in the fluid. The current interacts with the magnetic field to generate Lorentz force, thereby changing the movement of the fluid, and at the same time, the current causes a change in the electromagnetic field. The description of the complex behavior of the interaction between the conductive fluid and electromagnetic field generally uses the MHD equation, which is widely applied to describe the hydrodynamic behavior of conductive fluids such as plasma, liquid metal, and electrolyte (cf. [1–3]). Formally, the MHD system is a highly coupled nonlinear, saddle point structure system, that consists of the Navier-Stokes equations for hydrodynamics and Maxwell's equations for electromagnetism. The coupling of these two equations is achieved through the Lorentz force and fluid advection. Concerning the extensive theoretical modeling/analysis/simulations for the MHD system, we refer to [4–14] and the references therein. For example, positivity preserving analysis of density and pressure is carried

---

[*] Corresponding author.
E-mail addresses: gdzhang@ytu.edu.cn (G.-D. Zhang), hex@mst.edu (X. He), xfyang@math.sc.edu (X. Yang).

https://doi.org/10.1016/j.jcp.2021.110752

out in [5]; stochastic Galerkin method for ideal MHD system is proposed in [8]; a stabilized continuous Galerkin method for MHD problem is presented in [15].

In this paper, we consider the numerical approximation of the MHD system, focusing on establishing a fully-discrete finite element scheme with desired properties of linearity, second-order time accuracy, full decoupling structure, and unconditional energy stability (for simplicity, a numerical scheme with these properties is called as “desired” type scheme). Here, the linearity means only several linear problems are solved at each time step without requiring nonlinear iterations, while full decoupling means every unknown is solved independently. For the nonlinear coupled systems, the linear and fully decoupled algorithms are much more efficient compared with nonlinear coupled solvers. Then, a natural question is how difficult it is to design such a “desired” type scheme. One might think that it is not difficult because a large number of numerical methods have been developed to effectively handle this system [6,16–27] and the “desired” type scheme may be easily obtained by making some slight modifications to those schemes.

However, the opposite is true. Up to the authors’ knowledge, for the full MHD system, no scheme can meet all four criteria of the “desired” type scheme at the same time. For example, the schemes developed in [6,16] are either first-order time accurate with unconditional energy stability or second-order time accurate with conditional energy stability. The schemes developed in [21–23] are decoupled, have first-order time accuracy, and maintain energy stability conditionally. The first-order/second-order schemes developed in [24,25] can maintain unconditional energy stability with coupled structures. The schemes developed in [28,29] meet the requirements of full decoupling, unconditional energy stability, and linearity, but they are first-order time accurate. For the MHD model with simplified Lorentz force (ignoring the $\nabla(\frac{1}{2}|\mathbf{B}|^2)$ term), the “Elsässer” variable method developed in [18,19] lays a solid foundation and almost reaches the four features at the same time, while the unconditional stability is obtained under a condition of $\frac{1}{2} < \frac{\nu}{\eta} < 2$ (ν and η are diffusion coefficients in equations (2.11) and (2.13)). For the full MHD model considering $\nabla(\frac{1}{2}|\mathbf{B}|^2)$, the Elsässer variable method may not maintain the skew-symmetric structure of the nonlinear terms (see more details about this method in Remark 3.6).

Therefore, the focus of this paper is to construct a desired type fully-discrete numerical scheme for the highly complex, coupled, and nonlinear MHD model. The main challenge we need to overcome is how to develop a second-order time marching scheme with a decoupling structure under the premise of unconditional energy stability. To this end, while using several effective numerical methods, including the finite element method for spatial discretization, and the projection method for the Navier-Stokes equations, we have designed a new decoupling method that can effectively handle the coupling terms (advection and Lorentz force). By avoiding the traditional ways to distinguish which nonlinear items need to be processed explicitly or implicitly, we adopt a more direct principle to design the numerical scheme. That is, all nonlinear coupling items are handled using the second-order explicit extrapolation. It is well known that such a simple and crude explicit processing cannot obtain unconditional energy stability. Then, the key to overcome this issue is to use the “zero-energy-contribution” characteristics satisfied by those coupling terms. The specific approach is to introduce a nonlocal variable and design an appropriate ordinary differential equation (ODE), which consists of the inner products of the coupled terms with some specific functions. This ODE is trivial at the continuous level because all the terms contained in it provide a zero summation. But after discretization, it can help with obtaining unconditional energy stability. Meanwhile, the nonlocal variable can decompose each discrete equation into multiple sub-equations that can be solved independently and efficiently by using the fast solvers developed in [30,31], thereby obtaining a fully-decoupled structure.

Besides, the high efficiency of this scheme is also reflected in the fact that all variables can be calculated in a decoupled manner and all equations have constant coefficients at each time step. We also give rigorous proofs of the solvability and unconditional energy stability of the scheme. To demonstrate the stability and accuracy numerically, we further carry out several numerical examples, including the accurate/stability tests, and some MHD benchmark problems such as the hydromagnetic Kelvin-Helmholtz instability, driven cavity problems, to prove the effectiveness of the developed scheme, numerically. *To the authors’ best knowledge, for the MHD model, the constructed scheme is the first “desired” type scheme that can meet all four criteria at the same time, namely, it is fully-decoupled, second-order time accurate, linear and unconditionally energy stable.*

The “zero-energy-contribution” idea for constructing a decoupling scheme was recently published in [32–37] for the Navier-Stokes coupled gradient flow phase-field models. And the stability analysis was carried out only for the semi-discrete temporal schemes. In this paper, we consider a completely different type of flows, the MHD flows. Due to the major difficulty caused by the Maxwell’s equations, it is not trivial at all to utilize this idea to construct the nonlocal variable and carry out the corresponding analysis, for the MHD model. We also analyze the stability of the fully discrete finite element scheme, instead of the semi-discrete temporal scheme. Furthermore, the proposed decoupling technique through the nonlocal variable is also suitable to deal with the so-called H^1 discretization incompressible MHD system [7] (or called penalty MHD equations).

We organize the article in the following way. In Section 2, we briefly describe the MHD model and show its associated energy law. In Section 3, we construct the decoupled numerical scheme and present its detailed implementation steps. Unconditional energy stability and well-posedness are also proved rigorously. In Section 4, we present various 2D and 3D numerical simulations to demonstrate its stability and accuracy. Some concluding remarks are drawn in Section 5.

2. The MHD model and energy law

We study the incompressible MHD equations in a bounded domain $\Omega \subset R^d$, $d = 2, 3$ with connected boundary, that consist of the incompressible Navier-Stokes equations and the magnetoquasistatic Maxwell's equations, read as

$$\mathbf{u}_t - \nu\Delta\mathbf{u} + (\mathbf{u}\cdot\nabla)\mathbf{u} + \nabla p + \mathbf{B}\times\mathbf{J} = \mathbf{0}, \tag{2.1}$$

$$\text{div}\mathbf{u} = 0, \tag{2.2}$$

$$\mathbf{B}_t + \text{curl}\mathbf{E} = \mathbf{0}, \tag{2.3}$$

$$\frac{1}{\mu}\text{curl}\mathbf{B} = \mathbf{J}, \tag{2.4}$$

$$\mathbf{J} = \sigma(\mathbf{E} + \mathbf{u}\times\mathbf{B}), \tag{2.5}$$

$$\text{div}\mathbf{B} = 0, \tag{2.6}$$

where $\mathbf{u}$ is the fluid velocity, p is the hydrodynamic pressure, $\mathbf{E}$ is the electric field, $\mathbf{B}$ is the magnetic induction, $\mathbf{J}$ is the electric current density. The physical parameters ν, μ and σ are the kinematic viscosity, the magnetic permeability and the electric conductivity, respectively.

We plug (2.4) into (2.1) to get

$$\mathbf{u}_t - \nu\Delta\mathbf{u} + (\mathbf{u}\cdot\nabla)\mathbf{u} + \nabla p + \frac{1}{\mu}\mathbf{B}\times\text{curl}\mathbf{B} = \mathbf{0}. \tag{2.7}$$

Taking curl on the equations (2.4) and (2.5), we get

$$\text{curl}\mathbf{J} = \frac{1}{\mu}\text{curlcurl}\mathbf{B},$$
$$\text{curl}\mathbf{J} = \sigma\text{curl}\mathbf{E} + \sigma\text{curl}(\mathbf{u}\times\mathbf{B}),$$

which are combined together to get

$$\text{curl}\mathbf{E} = \frac{1}{\mu\sigma}\text{curlcurl}\mathbf{B} - \text{curl}(\mathbf{u}\times\mathbf{B}). \tag{2.8}$$

Then we plug (2.8) into (2.3) to obtain

$$\mathbf{B}_t + \frac{1}{\mu\sigma}\text{curlcurl}\mathbf{B} - \text{curl}(\mathbf{u}\times\mathbf{B}) = \mathbf{0}. \tag{2.9}$$

In [38], the equation (2.9) is modified to the following form

$$\mathbf{B}_t + \frac{1}{\mu\sigma}\text{curlcurl}\mathbf{B} - \text{curl}(\mathbf{u}\times\mathbf{B}) + \nabla r = \mathbf{0}, \quad r|_{\partial\Omega} = 0, \tag{2.10}$$

where r is the Lagrange multiplier term that is also called as “magnetic pressure”. Note that the modified equation (2.10) is indeed equivalent to (2.9). This is because if we apply divergence operator to (2.10) and use (2.6), we get $\Delta r = 0$. From the boundary condition for r, we deduce $r \equiv 0$. In this paper, we adopt (2.10) since this formulation allows us to use the second-order projection method, which was used to deal with the Navier-Stokes equations and can easily maintain the divergence-free condition for $\mathbf{B}$.

By denoting $\eta = \frac{1}{\mu\sigma}$, $\kappa = \frac{1}{\mu}$, we combine (2.2), (2.6), (2.7), and (2.10) to obtain the incompressible MHD equations that read as follows,

$$\mathbf{u}_t - \nu\Delta\mathbf{u} + (\mathbf{u}\cdot\nabla)\mathbf{u} + \nabla p + \kappa\mathbf{B}\times\text{curl}\mathbf{B} = \mathbf{0}, \tag{2.11}$$

$$\text{div}\mathbf{u} = 0, \tag{2.12}$$

$$\mathbf{B}_t + \eta\text{curlcurl}\mathbf{B} - \text{curl}(\mathbf{u}\times\mathbf{B}) + \nabla r = \mathbf{0}, \tag{2.13}$$

$$\text{div}\mathbf{B} = 0. \tag{2.14}$$

The system (2.11)-(2.14) is equipped with the following boundary conditions

$$\mathbf{u}|_{\partial\Omega} = \mathbf{0}, \quad \mathbf{B}\times\mathbf{n}|_{\partial\Omega} = \mathbf{0}, \quad r|_{\partial\Omega} = 0, \tag{2.15}$$

and initial conditions

$$\mathbf{u}|_{t=0} = \mathbf{u}_0, \quad \mathbf{B}|_{t=0} = \mathbf{B}_0, \tag{2.16}$$

with $\mathrm{div}\mathbf{u}_0 = 0$, $\mathrm{div}\mathbf{B}_0 = 0$, where $\mathbf{n}$ denotes the outward unit normal of $\partial\Omega$. In the literatures, $R_e = \nu^{-1}$ is called fluids Reynolds number, κ the coupling coefficient, and $R_m = \eta^{-1}$ the magnetic Reynolds number.

We first fix some notations here. For two vector functions $\mathbf{v}, \mathbf{w}$, we denote the L^2 inner product as $(\mathbf{v}, \mathbf{w}) = \int_\Omega \mathbf{v} \cdot \mathbf{w} d\mathbf{x}$ and the L^2 norm $\|\mathbf{w}\|^2 = (\mathbf{w}, \mathbf{w})$. Let $W^{k,l}(\Omega)$ stand for the standard Sobolev spaces equipped with the standard Sobolev norms $\|\cdot\|_{k,l}$. For $l = 2$, we write $H^k(\Omega)$ for $W^{k,2}(\Omega)$ and its corresponding norm is $\|\cdot\|_k$. We also list some function spaces for the MHD equations (2.11)-(2.16) as follows:

$$\begin{aligned}
&H^1(\Omega) = \left\{ w \in L^2(\Omega) : \nabla w \in L^2(\Omega)^d \right\}, \\
&H_0^1(\Omega) = \left\{ w \in H^1(\Omega) : w|_{\partial\Omega} = 0 \right\}, \\
&L_0^2(\Omega) = \left\{ q \in L^2(\Omega) : \int_\Omega q dx = 0 \right\}, \\
&\mathbf{H}^1(\Omega) = H^1(\Omega)^d, \ \ \mathbf{H}_0^1(\Omega) = H_0^1(\Omega)^d, \\
&H(\mathrm{curl}; \Omega) = \left\{ \mathbf{c} \in L^2(\Omega)^d : \mathrm{curl}\mathbf{c} \in L^2(\Omega)^{2d-3} \right\}, \\
&H_0(\mathrm{curl}; \Omega) = \{ \mathbf{c} \in H(\mathrm{curl}; \Omega) : \mathbf{c} \times \mathbf{n}|_{\partial\Omega} = \mathbf{0} \}.
\end{aligned}$$

The norm in $H(\mathrm{curl}; \Omega)$ space is defined by

$$\|\mathbf{c}\|_{\mathrm{curl}} = \left(\|\mathbf{c}\|^2 + \|\mathrm{curl}\mathbf{c}\|^2 \right)^{\frac{1}{2}}, \quad \forall \mathbf{c} \in H(\mathrm{curl}; \Omega).$$

The well-posedness and finite element approximation of steady version of the system (2.11)-(2.15) were discussed in [38]. Here, we also give a brief proof of the energy law followed by the MHD system (2.11)-(2.16), because the energy stability of the discrete scheme follows the same line. By taking the L^2 inner product of $\mathbf{u}$ with (2.11) and using the integration by parts and (2.12), we get

$$\frac{1}{2}\frac{d}{dt}\|\mathbf{u}\|^2 + \nu\|\nabla\mathbf{u}\|^2 + \int_\Omega (\mathbf{u} \cdot \nabla)\mathbf{u} \cdot \mathbf{u} d\mathbf{x} + \kappa \int_\Omega (\mathbf{B} \times \mathrm{curl}\mathbf{B}) \cdot \mathbf{u} d\mathbf{x} = 0. \tag{2.17}$$

Taking the L^2 inner product of $\kappa\mathbf{B}$ with (2.13), and using the integration by parts and (2.14), we have

$$\frac{\kappa}{2}\frac{d}{dt}\|\mathbf{B}\|^2 + \kappa\eta\|\mathrm{curl}\mathbf{B}\|^2 - \kappa \int_\Omega \mathrm{curl}(\mathbf{u} \times \mathbf{B}) \cdot \mathbf{B} d\mathbf{x} = 0. \tag{2.18}$$

By combining (2.17) and (2.18), we obtain the law of energy dissipation that reads as:

$$\frac{d}{dt}(\frac{1}{2}\|\mathbf{u}\|^2 + \frac{\kappa}{2}\|\mathbf{B}\|^2) = -\nu\|\nabla\mathbf{u}\|^2 - \kappa\eta\|\mathrm{curl}\mathbf{B}\|^2 \leq 0. \tag{2.19}$$

Remark 2.1. The above proof to obtain the law of energy dissipation (2.19) lies on the following two identities:

$$\int_\Omega (\mathbf{u} \cdot \nabla)\mathbf{u} \cdot \mathbf{u} d\mathbf{x} = 0, \quad \int_\Omega [(\mathbf{B} \times \mathrm{curl}\mathbf{B}) \cdot \mathbf{u} - \mathbf{u} \times \mathbf{B} \cdot \mathrm{curl}\mathbf{B}] \, d\mathbf{x} = 0.$$

These equalities are derived by using the integration by parts and the boundary conditions for $\mathbf{u}$. These two equalities can be regarded as the contribution of two types of nonlinear terms (advection and Lorentz force) to the total free energy of the system is zero. These unique "zero-energy-contribution" property will be used to design decoupling type numerical schemes.

3. Numerical scheme

In this section, we aim to construct a "desired" type fully-discrete finite element scheme to solve the MHD system (2.11)-(2.16). The most critical technique for this goal is to follow the "zero-energy-contribution" idea [36,37]. Special processing is needed to develop appropriate temporal discretizations for the challenging terms, including the coupling terms of advection and Lorentz force, and the linear coupling between velocity and pressure through the divergence-free condition.

3.1. Reformulated equivalent system and energy law

In order to design the desired algorithm, we introduce a nonlocal scalar variable $Q(t)$ and its corresponding ODE, and we rewrite the MHD equations (2.11)-(2.16) to an augmented equivalent form.

We introduce a nonlocal variable $Q(t)$ and design an ODE system for it, that reads as:

$$\begin{cases} Q_t = \int\limits_\Omega (\mathbf{u}\cdot\nabla)\mathbf{u}\cdot\mathbf{u}d\mathbf{x} + \kappa\int\limits_\Omega \mathbf{B}\times\text{curl}\mathbf{B}\cdot\mathbf{u}d\mathbf{x} - \kappa\int\limits_\Omega \mathbf{u}\times\mathbf{B}\cdot\text{curl}\mathbf{B}d\mathbf{x}, \\ Q|_{t=0} = 1. \end{cases} \tag{3.1}$$

It is easy to see that the system (3.1) is the same as a trivial ODE system of $Q_t = 0$, $Q|_{t=0} = 1$ with the exact solution of $Q(t) = 1$.

We rewrite the MHD system (2.11)-(2.16) using the new variable Q to the following form:

$$\mathbf{u}_t - \nu\Delta\mathbf{u} + Q(\mathbf{u}\cdot\nabla)\mathbf{u} + \nabla p + Q\kappa\mathbf{B}\times\text{curl}\mathbf{B} = \mathbf{0}, \tag{3.2}$$

$$\text{div}\mathbf{u} = 0, \tag{3.3}$$

$$\mathbf{B}_t + \eta\text{curlcurl}\mathbf{B} - Q\,\text{curl}(\mathbf{u}\times\mathbf{B}) + \nabla r = \mathbf{0}, \tag{3.4}$$

$$\text{div}\mathbf{B} = 0, \tag{3.5}$$

$$Q_t = \int\limits_\Omega (\mathbf{u}\cdot\nabla)\mathbf{u}\cdot\mathbf{u}d\mathbf{x} + \kappa\int\limits_\Omega \mathbf{B}\times\text{curl}\mathbf{B}\cdot\mathbf{u}d\mathbf{x} - \kappa\int\limits_\Omega \mathbf{u}\times\mathbf{B}\cdot\text{curl}\mathbf{B}d\mathbf{x}, \tag{3.6}$$

$$\mathbf{u}|_{\partial\Omega} = \mathbf{0}, \quad \mathbf{B}\times\mathbf{n}|_{\partial\Omega} = \mathbf{0}, \quad r|_{\partial\Omega} = 0, \tag{3.7}$$

$$\mathbf{u}|_{t=0} = \mathbf{u}_0, \quad \mathbf{B}|_{t=0} = \mathbf{B}_0, \quad Q|_{t=0} = 1. \tag{3.8}$$

Remark 3.1. We multiply the advection terms ($(\mathbf{u}\cdot\nabla)\mathbf{u}$ and $\text{curl}(\mathbf{u}\times\mathbf{B})$), and Lorentz force $\kappa\mathbf{B}\times\text{curl}\mathbf{B}$ with Q. Since the nonlocal variable $Q(t)$ is equal to 1, the PDE system will not be changed by this modification. Therefore, the two PDE systems, (2.11)-(2.16) and (3.2)-(3.8) are equivalent.

Theorem 3.1. *The transformed MHD system* (3.2)-(3.8) *admits the following law of energy dissipation*

$$\frac{d}{dt}\left(\frac{1}{2}\|\mathbf{u}\|^2 + \frac{\kappa}{2}\|\mathbf{B}\|^2 + \frac{1}{2}|Q|^2\right) = -\nu\|\nabla\mathbf{u}\|^2 - \kappa\eta\|\text{curl}\mathbf{B}\|^2 \le 0. \tag{3.9}$$

Proof. Taking the L^2 inner product of $\mathbf{u}$ with (3.2) and using the integration by parts, we obtain

$$\frac{1}{2}\frac{d}{dt}\|\mathbf{u}\|^2 + \nu\|\nabla\mathbf{u}\|^2 + Q\int\limits_\Omega (\mathbf{u}\cdot\nabla)\mathbf{u}\cdot\mathbf{u}d\mathbf{x} + \kappa Q\int\limits_\Omega \mathbf{B}\times\text{curl}\mathbf{B}\cdot\mathbf{u}d\mathbf{x} = 0. \tag{3.10}$$

Taking the L^2 inner product of $\kappa\mathbf{B}$ with (3.4) and using the integration by parts, we obtain

$$\frac{\kappa}{2}\frac{d}{dt}\|\mathbf{B}\|^2 + \kappa\eta\|\text{curl}\mathbf{B}\|^2 - \kappa Q\int\limits_\Omega \mathbf{u}\times\mathbf{B}\cdot\text{curl}\mathbf{B}d\mathbf{x} = 0. \tag{3.11}$$

Multiplying Q on (3.6) leads to

$$\begin{aligned} \frac{1}{2}\frac{d}{dt}|Q|^2 = {} & Q\int\limits_\Omega (\mathbf{u}\cdot\nabla)\mathbf{u}\cdot\mathbf{u}d\mathbf{x} + \kappa Q\int\limits_\Omega \mathbf{B}\times\text{curl}\mathbf{B}\cdot\mathbf{u}d\mathbf{x} \\ & - \kappa Q\int\limits_\Omega \mathbf{u}\times\mathbf{B}\cdot\text{curl}\mathbf{B}d\mathbf{x}. \end{aligned} \tag{3.12}$$

By combining (3.10) - (3.12), we derive (3.9).

3.2. Fully-discrete decoupled finite element scheme

We develop the fully discrete finite element scheme for the transformed equivalent model (3.2)-(3.8) in this subsection.

The weak form of the system (3.2)-(3.8) reads as: find $\mathbf{u}(t) \in \mathbf{H}_0^1(\Omega)$, $p(t) \in L_0^2(\Omega)$, $\mathbf{B}(t) \in H_0(\text{curl};\Omega)$, and $r(t) \in H_0^1(\Omega)$ such that

$$(\mathbf{u}_t, \mathbf{v}) + \nu(\nabla \mathbf{u}, \nabla \mathbf{v}) + Q((\mathbf{u}\cdot\nabla)\mathbf{u}, \mathbf{v}) - (p, \text{div}\mathbf{v}) + Q\kappa(\mathbf{B}\times\text{curl}\mathbf{B}, \mathbf{v}) = 0, \tag{3.13}$$

$$(\text{div}\mathbf{u}, q) = 0, \tag{3.14}$$

$$(\mathbf{B}_t, \mathbf{c}) + \eta(\text{curl}\mathbf{B}, \text{curl}\mathbf{c}) - Q(\mathbf{u}\times\mathbf{B}, \text{curl}\mathbf{c}) + (\nabla r, \mathbf{c}) = 0, \tag{3.15}$$

$$(\mathbf{B}, \nabla s) = 0, \tag{3.16}$$

$$Q_t = \int_\Omega (\mathbf{u}\cdot\nabla)\mathbf{u}\cdot\mathbf{u}d\mathbf{x} + \kappa\int_\Omega \mathbf{B}\times\text{curl}\mathbf{B}\cdot\mathbf{u}d\mathbf{x} - \kappa\int_\Omega \mathbf{u}\times\mathbf{B}\cdot\text{curl}\mathbf{B}d\mathbf{x}, \tag{3.17}$$

for all $\mathbf{v} \in \mathbf{H}_0^1(\Omega)$, $q \in L_0^2(\Omega)$, $\mathbf{c} \in H_0(\text{curl};\Omega)$, and $s \in H_0^1(\Omega)$.

We adopt the finite element method for the spatial discretization. We consider regular and quasi-uniform meshes $\mathcal{T}_h$ of mesh-size h that partition Ω into triangle or tetrahedra $\{K\}$. Let $\mathcal{P}_l(K)$ be the space of polynomials of total degree at most l on K and $\tilde{\mathcal{P}}_l(K)$ the space of homogeneous polynomials of degree l. The space $\mathcal{D}_l(K)$ denotes the polynomials $\tilde{\mathbf{p}}$ in $\tilde{\mathcal{P}}_l(K)^d$ that satisfy $\tilde{\mathbf{p}}\cdot\mathbf{x} = 0$ on K. For $l \geq 1$, we define the space $\mathcal{N}_l(K) = \mathcal{P}_{l-1}(K)^d \oplus \mathcal{D}_l(K)$. We apply standard Lagrange finite element spaces $\mathbf{V}_h$ and M_h to approximate unknowns in $\mathbf{H}_0^1(\Omega)$ and $L_0^2(\Omega)$, see [39],

$$\mathbf{V}_h = \left\{\mathbf{v}_h \in \mathbf{H}_0^1(\Omega) : \mathbf{v}_h|_K \in \mathcal{P}_{l+1}(K)^d, K \in \mathcal{T}_h\right\},$$
$$M_h = \left\{q_h \in L_0^2(\Omega) : q_h|_K \in \mathcal{P}_l(K), K \in \mathcal{T}_h\right\}.$$

Moreover, the spaces $\mathbf{V}_h$ and M_h need to satisfy the *inf-sup* condition:

$$\beta\|q_h\| \leq \sup_{\mathbf{v}_h\in\mathbf{V}_h} \frac{(\text{div}\mathbf{v}_h, q_h)}{\|\nabla\mathbf{v}_h\|}, \quad \forall q_h \in M_h. \tag{3.18}$$

To approximate unknowns in $H_0(\text{curl};\Omega)$ and $H_0^1(\Omega)$, we use the first family of Nédélec space [40,41] and Lagrange finite element space,

$$\mathbf{C}_h = \{\mathbf{c}_h \in H_0(\text{curl};\Omega) : \mathbf{c}_h|_K \in \mathcal{N}_l(K), K \in \mathcal{T}_h\},$$
$$S_h = \left\{s_h \in H_0^1(\Omega) : s_h|_K \in \mathcal{P}_l(K), K \in \mathcal{T}_h\right\}.$$

Furthermore, the pair $\mathbf{C}_h$ and S_h require to satisfy $\nabla S_h \subset \mathbf{C}_h$, which also means the *inf-sup* condition:

$$\hat{\beta}\|s_h\|_1 \leq \sup_{\mathbf{c}_h\in\mathbf{C}_h} \frac{(\mathbf{c}_h, \nabla s_h)}{\|\mathbf{c}_h\|_{\text{curl}}}, \quad \forall s_h \in S_h. \tag{3.19}$$

Some well known *inf-sup* stable pairs for $(\mathbf{V}_h, M_h)$ and $(\mathbf{C}_h, S_h)$ are available, see [39,41,38].

We define extrapolation $\mathbf{w}_h^* = 2\mathbf{w}_h^n - \mathbf{w}_h^{n-1}$ for any variable $\mathbf{w}_h$. We use the second-order pressure projection method to decouple the linear couplings of $(\mathbf{u}, p)$ and $(\mathbf{B}, r)$, and the second-order backward differentiation formula (BDF2) for the temporal discretization. Let $\delta t > 0$ denote the time step size and set $t_n = n\delta t$ for $0 \leq n \leq N$ with $T = N\delta t$. The fully discrete scheme to solve the system (3.13)-(3.17) reads as follows:

Find $\tilde{\mathbf{u}}_h^{n+1} \in \mathbf{V}_h$, $\mathbf{u}_h^{n+1} \in \mathbf{V}_h + \nabla M_h$, $p_h^{n+1} \in M_h$, $\tilde{\mathbf{B}}_h^{n+1} \in \mathbf{C}_h$, $\mathbf{B}_h^{n+1} \in \mathbf{C}_h + \nabla S_h$, $r_h^{n+1} \in S_h$ such that

$$\begin{aligned}&\left(\frac{a\tilde{\mathbf{u}}_h^{n+1} - b\mathbf{u}_h^n + c\mathbf{u}_h^{n-1}}{2\delta t}, \mathbf{v}_h\right) + \nu(\nabla\tilde{\mathbf{u}}_h^{n+1}, \nabla\mathbf{v}_h) + (\nabla p_h^n, \mathbf{v}_h)\\ &\qquad + Q^{n+1}((\mathbf{u}_h^*\cdot\nabla)\mathbf{u}_h^*, \mathbf{v}_h) + \kappa Q^{n+1}(\mathbf{B}_h^*\times\text{curl}\mathbf{B}_h^*, \mathbf{v}_h) = 0,\end{aligned} \tag{3.20}$$

$$\begin{aligned}&\left(\frac{a\tilde{\mathbf{B}}_h^{n+1} - b\mathbf{B}_h^n + c\mathbf{B}_h^{n-1}}{2\delta t}, \mathbf{c}_h\right) + \eta(\text{curl}\tilde{\mathbf{B}}_h^{n+1}, \text{curl}\mathbf{c}_h)\\ &\qquad - Q^{n+1}(\mathbf{u}_h^*\times\mathbf{B}_h^*, \text{curl}\mathbf{c}_h) + (\nabla r_h^n, \mathbf{c}_h) = 0,\end{aligned} \tag{3.21}$$

$$\frac{aQ^{n+1} - bQ^n + cQ^{n-1}}{2\delta t} = \int_\Omega (\mathbf{u}_h^*\cdot\nabla)\mathbf{u}_h^*\cdot\tilde{\mathbf{u}}_h^{n+1}d\mathbf{x} \tag{3.22}$$

$$+\kappa\int_\Omega \mathbf{B}_h^*\times \mathrm{curl}\mathbf{B}_h^*\cdot\tilde{\mathbf{u}}_h^{n+1}d\mathbf{x}-\kappa\int_\Omega \mathbf{u}_h^*\times\mathbf{B}_h^*\cdot\mathrm{curl}\tilde{\mathbf{B}}_h^{n+1}d\mathbf{x},$$

$$(\nabla p_h^{n+1},\nabla q_h)=-\frac{a}{2\delta t}(\mathrm{div}\tilde{\mathbf{u}}_h^{n+1},q_h)+(\nabla p_h^n,\nabla q_h),\tag{3.23}$$

$$\mathbf{u}_h^{n+1}=\tilde{\mathbf{u}}_h^{n+1}-\frac{2}{a}\delta t\nabla p_h^{n+1}+\frac{2}{a}\delta t\nabla p_h^n,\tag{3.24}$$

$$(\nabla r_h^{n+1},\nabla s_h)=\frac{a}{2\delta t}(\tilde{\mathbf{B}}_h^{n+1},\nabla s_h)+(\nabla r_h^n,\nabla s_h).\tag{3.25}$$

$$\mathbf{B}_h^{n+1}=\tilde{\mathbf{B}}_h^{n+1}-\frac{2}{a}\delta t\nabla r_h^{n+1}+\frac{2}{a}\delta t\nabla r_h^n,\tag{3.26}$$

for all $\mathbf{v}_h\in\mathbf{V}_h, \mathbf{c}_h\in\mathbf{C}_h, q_h\in M_h, s_h\in S_h$, where $a=3, b=4, c=1$.

Several remarks are in order.

Remark 3.1. The second-order pressure-projection method is used to decouple the computations of the linear couplings of $(\mathbf{u},p)$ and $(\mathbf{B},r)$. It is shown in [42] that the L^2 error of velocity can achieve the second-order time accuracy, while the L^2 error of pressure and H^1 error of velocity can only achieve first-order time accuracy. The loss of accuracy for pressure is due to the artificial Neumann boundary condition imposed on the pressure, see [43].

Remark 3.2. The final velocity field $\mathbf{u}_h^{n+1}$ in above scheme satisfies the weakly discrete divergence-free condition. This can be deduced as follows. By taking the L^2 inner product of (3.24) with ∇q_h, $\forall q_h\in M_h$, we obtain

$$(\mathbf{u}_h^{n+1},\nabla q_h)=-(\mathrm{div}\tilde{\mathbf{u}}_h^{n+1},q_h)-\frac{2}{a}\delta t(\nabla(p_h^{n+1}-p_h^n),\nabla q_h).$$

In view of (3.23), we arrive at

$$(\mathbf{u}_h^{n+1},\nabla q_h)=0,\ \ \forall q_h\in M_h.\tag{3.27}$$

Likewise, we also have

$$(\mathbf{B}_h^{n+1},\nabla s_h)=(\tilde{\mathbf{B}}_h^{n+1},\nabla s_h)-\frac{2}{a}\delta t(\nabla r_h^{n+1}-\nabla r_h^n,\nabla s_h)=0,\quad \forall s_h\in S_h.\tag{3.28}$$

Remark 3.3. The above scheme also needs the first step solution $\mathbf{u}_h^1$, p_h^1, $\mathbf{B}_h^1$, r_h^1 and Q^1 that can be easily obtained from the first order scheme by setting $n=0, a=2, b=2, c=0$ and $\mathbf{u}_h^*=\mathbf{u}_h^0$, $\mathbf{B}_h^*=\mathbf{B}_h^0$ in (3.20)-(3.26).

Remark 3.4. In the pressure projection decoupled method, the initial data of pressure p is often set zero, which may cause numerical errors or instability. A more reliable way is to compute the system at $t=t_1$ using a coupled scheme to obtain $(\mathbf{u}_h^1, p_h^1, \mathbf{B}_h^1, r_h^1)$. Then the pressure projection decoupled scheme is implemented from $t=t_2$ and initialized by the solution at $t=t_1$.

We now prove the energy stability of the scheme (3.20)-(3.26).

Theorem 3.2. *The scheme* (3.20)-(3.26) *holds the unconditional energy stability in the sense that*

$$E^{n+1}\le E^n-2\delta t\nu\|\nabla\tilde{\mathbf{u}}_h^{n+1}\|^2-2\delta t\kappa\eta\|\mathrm{curl}\tilde{\mathbf{B}}_h^{n+1}\|^2,\tag{3.29}$$

where

$$\begin{aligned}E^{n+1}=&\frac{1}{2}(\|\mathbf{u}_h^{n+1}\|^2+\|2\mathbf{u}_h^{n+1}-\mathbf{u}_h^n\|^2)+\frac{\kappa}{2}(\|\mathbf{B}_h^{n+1}\|^2+\|2\mathbf{B}_h^{n+1}-\mathbf{B}_h^n\|^2)\\&+\frac{1}{2}(|Q^{n+1}|^2+|2Q^{n+1}-Q^n|^2)+\frac{2\delta t^2}{3}\|\nabla p_h^{n+1}\|^2+\frac{2\kappa\delta t^2}{3}\|\nabla r_h^{n+1}\|^2.\end{aligned}\tag{3.30}$$

Proof. Taking $\mathbf{v}_h=\tilde{\mathbf{u}}_h^{n+1}$ in (3.20), we have

$$\begin{aligned}&\left(\frac{3\tilde{\mathbf{u}}_h^{n+1}-4\mathbf{u}_h^n+\mathbf{u}_h^{n-1}}{2\delta t},\tilde{\mathbf{u}}_h^{n+1}\right)+\nu\|\nabla\tilde{\mathbf{u}}_h^{n+1}\|^2+(\nabla p_h^n,\tilde{\mathbf{u}}_h^{n+1})\\&+Q^{n+1}\int_\Omega(\mathbf{u}_h^*\cdot\nabla)\mathbf{u}_h^*\cdot\tilde{\mathbf{u}}_h^{n+1}d\mathbf{x}+\kappa Q^{n+1}\int_\Omega(\mathbf{B}_h^*\times\mathrm{curl}\mathbf{B}_h^*)\cdot\tilde{\mathbf{u}}_h^{n+1}d\mathbf{x}=0.\end{aligned}\tag{3.31}$$

Taking $\mathbf{c}_h = \kappa \tilde{\mathbf{B}}_h^{n+1}$ in (3.21), we obtain

$$\begin{aligned}\kappa\left(\frac{3\tilde{\mathbf{B}}_h^{n+1} - 4\mathbf{B}_h^n + \mathbf{B}_h^{n-1}}{2\delta t}, \tilde{\mathbf{B}}_h^{n+1}\right) + \kappa\eta\|\mathrm{curl}\tilde{\mathbf{B}}_h^{n+1}\|^2 + \kappa(\nabla r_h^n, \tilde{\mathbf{B}}_h^{n+1})\\ - \kappa Q^{n+1}\int_\Omega (\mathbf{u}_h^* \times \mathbf{B}_h^*)\cdot \mathrm{curl}\tilde{\mathbf{B}}_h^{n+1} d\mathbf{x} = 0.\end{aligned} \tag{3.32}$$

Multiplying (3.22) with Q^{n+1}, we have

$$\begin{aligned}\frac{1}{2\delta t}(3Q^{n+1} - 4Q^n + Q^{n-1})Q^{n+1} = Q^{n+1}\int_\Omega (\mathbf{u}_h^* \cdot \nabla)\mathbf{u}_h^* \cdot \tilde{\mathbf{u}}_h^{n+1} d\mathbf{x}\\ + \kappa Q^{n+1}\int_\Omega (\mathbf{B}_h^* \times \mathrm{curl}\mathbf{B}_h^*)\cdot \tilde{\mathbf{u}}_h^{n+1} d\mathbf{x}\\ - \kappa Q^{n+1}\int_\Omega (\mathbf{u}_h^* \times \mathbf{B}_h^*)\cdot \mathrm{curl}\tilde{\mathbf{B}}_h^{n+1} d\mathbf{x}.\end{aligned} \tag{3.33}$$

Summing up (3.31)-(3.33), we obtain

$$\begin{aligned}&\frac{1}{2\delta t}(3\tilde{\mathbf{u}}_h^{n+1} - 4\mathbf{u}_h^n + \mathbf{u}_h^{n-1}, \tilde{\mathbf{u}}_h^{n+1}) + \frac{\kappa}{2\delta t}(3\tilde{\mathbf{B}}_h^{n+1} - 4\mathbf{B}_h^n + \mathbf{B}_h^{n-1}, \tilde{\mathbf{B}}_h^{n+1})\\ &\quad + \nu\|\nabla\tilde{\mathbf{u}}_h^{n+1}\|^2 + \kappa\eta\|\mathrm{curl}\tilde{\mathbf{B}}_h^{n+1}\|^2 + \frac{1}{2\delta t}(3Q^{n+1} - 4Q^n + Q^{n-1})Q^{n+1}\\ &\quad + (\nabla p_h^n, \tilde{\mathbf{u}}_h^{n+1}) + \kappa(\nabla r_h^n, \tilde{\mathbf{B}}_h^{n+1}) = 0.\end{aligned} \tag{3.34}$$

From (3.24), (3.27), (3.26), and (3.28), we have

$$(\mathbf{u}_h^{n+1} - \tilde{\mathbf{u}}_h^{n+1}, \mathbf{u}_h^{n+1}) = -\frac{2}{3}\delta t(\nabla p_h^{n+1} - \nabla p_h^n, \mathbf{u}_h^{n+1}) = 0, \tag{3.35}$$

$$(\mathbf{B}_h^{n+1} - \tilde{\mathbf{B}}_h^{n+1}, \mathbf{B}_h^{n+1}) = -\frac{2}{3}\delta t(\nabla r_h^{n+1} - \nabla r_h^n, \mathbf{B}_h^{n+1}) = 0. \tag{3.36}$$

Thus, by using (3.35), (3.36), and the following identity

$$2(3\hat{a} - 4\hat{b} + \hat{c})\hat{a} = |\hat{a}|^2 - |\hat{b}|^2 + |2\hat{a} - \hat{b}|^2 - |2\hat{b} - \hat{c}|^2 + |\hat{a} - 2\hat{b} + \hat{c}|^2, \tag{3.37}$$

we derive

$$\begin{aligned}&(3\tilde{\mathbf{u}}_h^{n+1} - 4\mathbf{u}_h^n + \mathbf{u}_h^{n-1}, \tilde{\mathbf{u}}_h^{n+1})\\ &\quad =(3\mathbf{u}_h^{n+1} - 4\mathbf{u}_h^n + \mathbf{u}_h^{n-1}, \tilde{\mathbf{u}}_h^{n+1}) + (3\tilde{\mathbf{u}}_h^{n+1} - 3\mathbf{u}_h^{n+1}, \tilde{\mathbf{u}}_h^{n+1})\\ &\quad =(3\mathbf{u}_h^{n+1} - 4\mathbf{u}_h^n + \mathbf{u}_h^{n-1}, \mathbf{u}_h^{n+1}) + (3\tilde{\mathbf{u}}_h^{n+1} - 3\mathbf{u}_h^{n+1}, \tilde{\mathbf{u}}_h^{n+1} + \mathbf{u}_h^{n+1})\\ &\quad =\frac{1}{2}(\|\mathbf{u}_h^{n+1}\|^2 - \|\mathbf{u}_h^n\|^2 + \|2\mathbf{u}_h^{n+1} - \mathbf{u}_h^n\|^2 - \|2\mathbf{u}_h^n - \mathbf{u}_h^{n-1}\|^2\\ &\qquad + \|\mathbf{u}_h^{n+1} - 2\mathbf{u}_h^n + \mathbf{u}_h^{n-1}\|^2) + 3\|\tilde{\mathbf{u}}_h^{n+1}\|^2 - 3\|\mathbf{u}_h^{n+1}\|^2,\end{aligned} \tag{3.38}$$

$$\begin{aligned}&(3\tilde{\mathbf{B}}_h^{n+1} - 4\mathbf{B}_h^n + \mathbf{B}_h^{n-1}, \tilde{\mathbf{B}}_h^{n+1})\\ &\quad =(3\mathbf{B}_h^{n+1} - 4\mathbf{B}_h^n + \mathbf{B}_h^{n-1}, \tilde{\mathbf{B}}_h^{n+1}) + (3\tilde{\mathbf{B}}_h^{n+1} - 3\mathbf{B}_h^{n+1}, \tilde{\mathbf{B}}_h^{n+1})\\ &\quad =(3\mathbf{B}_h^{n+1} - 4\mathbf{B}_h^n + \mathbf{B}_h^{n-1}, \mathbf{B}_h^{n+1}) + (3\tilde{\mathbf{B}}_h^{n+1} - 3\mathbf{B}_h^{n+1}, \tilde{\mathbf{B}}_h^{n+1} + \mathbf{B}_h^{n+1})\\ &\quad =\frac{1}{2}(\|\mathbf{B}_h^{n+1}\|^2 - \|\mathbf{B}_h^n\|^2 + \|2\mathbf{B}_h^{n+1} - \mathbf{B}_h^n\|^2 - \|2\mathbf{B}_h^n - \mathbf{B}_h^{n-1}\|^2\\ &\qquad + \|\mathbf{B}_h^{n+1} - 2\mathbf{B}_h^n + \mathbf{B}_h^{n-1}\|^2) + 3\|\tilde{\mathbf{B}}_h^{n+1}\|^2 - 3\|\mathbf{B}_h^{n+1}\|^2,\end{aligned} \tag{3.39}$$

and

$$\begin{aligned}\frac{1}{2\delta t}(3Q^{n+1} - 4Q^n + Q^{n-1})Q^{n+1} = \frac{1}{4\delta t}(|Q^{n+1}|^2 - |Q^n|^2 + |2Q^{n+1} - Q^n|^2\\ - |2Q^n - Q^{n-1}|^2 + |Q^{n+1} - 2Q^n + Q^{n-1}|^2).\end{aligned} \tag{3.40}$$

From (3.24) and (3.26), we obtain

$$\mathbf{u}_h^{n+1} + \frac{2}{3}\delta t\nabla p_h^{n+1} = \tilde{\mathbf{u}}_h^{n+1} + \frac{2}{3}\delta t\nabla p_h^n, \tag{3.41}$$

$$\mathbf{B}_h^{n+1} + \frac{2}{3}\delta t\nabla r_h^{n+1} = \tilde{\mathbf{B}}_h^{n+1} + \frac{2}{3}\delta t\nabla r_h^n. \tag{3.42}$$

Taking the L^2 inner product of the above two equations with themselves, and using (3.27) and (3.28), we have

$$(\tilde{\mathbf{u}}_h^{n+1}, \nabla p^n) = \frac{3}{4\delta t}\|\mathbf{u}^{n+1}\|^2 - \frac{3}{4\delta t}\|\tilde{\mathbf{u}}_h^{n+1}\|^2 + \frac{\delta t}{3}\|\nabla p^{n+1}\|^2 - \frac{\delta t}{3}\|\nabla p^n\|^2, \tag{3.43}$$

$$(\tilde{\mathbf{B}}_h^{n+1}, \nabla r^n) = \frac{3}{4\delta t}\|\mathbf{B}^{n+1}\|^2 - \frac{3}{4\delta t}\|\tilde{\mathbf{B}}_h^{n+1}\|^2 + \frac{\delta t}{3}\|\nabla r^{n+1}\|^2 - \frac{\delta t}{3}\|\nabla r^n\|^2. \tag{3.44}$$

Combining (3.34) with (3.38), (3.39), (3.40), (3.43), (3.44), we derive

$$\begin{aligned}
&\frac{1}{4\delta t}(\|\mathbf{u}_h^{n+1}\|^2 - \|\mathbf{u}_h^n\|^2 + \|2\mathbf{u}_h^{n+1} - \mathbf{u}_h^n\|^2 - \|2\mathbf{u}_h^n - \mathbf{u}_h^{n-1}\|^2 + \|\mathbf{u}_h^{n+1} - 2\mathbf{u}_h^n + \mathbf{u}_h^{n-1}\|^2)\\
&\quad + \frac{\kappa}{4\delta t}(\|\mathbf{B}_h^{n+1}\|^2 - \|\mathbf{B}_h^n\|^2 + \|2\mathbf{B}_h^{n+1} - \mathbf{B}_h^n\|^2 - \|2\mathbf{B}_h^n - \mathbf{B}_h^{n-1}\|^2\\
&\quad + \|\mathbf{B}_h^{n+1} - 2\mathbf{B}_h^n + \mathbf{B}_h^{n-1}\|^2)\\
&\quad + \frac{1}{4\delta t}(|Q^{n+1}|^2 - |Q^n|^2 + |2Q^{n+1} - Q^n|^2 - |2Q^n - Q^{n-1}|^2\\
&\quad + |Q^{n+1} - 2Q^n + Q^{n-1}|^2)\\
&\quad + \frac{\delta t}{3}\|\nabla p_h^{n+1}\|^2 - \frac{\delta t}{3}\|\nabla p_h^n\|^2 + \frac{\kappa\delta t}{3}\|\nabla r_h^{n+1}\|^2 - \frac{\kappa\delta t}{3}\|\nabla r_h^n\|^2\\
&\quad + \frac{3}{4\delta t}\|\tilde{\mathbf{u}}_h^{n+1}\|^2 - \frac{3}{4\delta t}\|\mathbf{u}_h^{n+1}\|^2 + \frac{3\kappa}{4\delta t}\|\tilde{\mathbf{B}}_h^{n+1}\|^2 - \frac{3\kappa}{4\delta t}\|\mathbf{B}_h^{n+1}\|^2\\
&\quad = -\nu\|\nabla\tilde{\mathbf{u}}_h^{n+1}\|^2 - \kappa\eta\|\mathrm{curl}\tilde{\mathbf{B}}_h^{n+1}\|^2.
\end{aligned} \tag{3.45}$$

From (3.35) and (3.36), we derive

$$\begin{aligned}
\|\tilde{\mathbf{u}}_h^{n+1}\|^2 - \|\mathbf{u}_h^{n+1}\|^2 &= (\tilde{\mathbf{u}}_h^{n+1} - \mathbf{u}_h^{n+1}, \tilde{\mathbf{u}}_h^{n+1} + \mathbf{u}_h^{n+1})\\
&= (\tilde{\mathbf{u}}_h^{n+1} - \mathbf{u}_h^{n+1}, \tilde{\mathbf{u}}_h^{n+1} + \mathbf{u}_h^{n+1} - 2\mathbf{u}_h^{n+1})\\
&= \|\tilde{\mathbf{u}}_h^{n+1} - \mathbf{u}_h^{n+1}\|^2,
\end{aligned} \tag{3.46}$$

and

$$\begin{aligned}
\|\tilde{\mathbf{B}}_h^{n+1}\|^2 - \|\mathbf{B}_h^{n+1}\|^2 &= (\tilde{\mathbf{B}}_h^{n+1} - \mathbf{B}_h^{n+1}, \tilde{\mathbf{B}}_h^{n+1} + \mathbf{B}_h^{n+1})\\
&= (\tilde{\mathbf{B}}_h^{n+1} - \mathbf{B}_h^{n+1}, \tilde{\mathbf{B}}_h^{n+1} + \mathbf{B}_h^{n+1} - 2\mathbf{B}_h^{n+1})\\
&= \|\tilde{\mathbf{B}}_h^{n+1} - \mathbf{B}_h^{n+1}\|^2.
\end{aligned} \tag{3.47}$$

Finally, combining (3.45), (3.46), (3.47) with multiplying $2\delta t$, we obtain

$$\begin{aligned}
&\frac{1}{2}(\|\mathbf{u}_h^{n+1}\|^2 - \|\mathbf{u}_h^n\|^2 + \|2\mathbf{u}_h^{n+1} - \mathbf{u}_h^n\|^2 - \|2\mathbf{u}_h^n - \mathbf{u}_h^{n-1}\|^2 + \|\mathbf{u}_h^{n+1} - 2\mathbf{u}_h^n + \mathbf{u}_h^{n-1}\|^2)\\
&\quad + \frac{\kappa}{2}(\|\mathbf{B}_h^{n+1}\|^2 - \|\mathbf{B}_h^n\|^2 + \|2\mathbf{B}_h^{n+1} - \mathbf{B}_h^n\|^2 - \|2\mathbf{B}_h^n - \mathbf{B}_h^{n-1}\|^2\\
&\quad + \|\mathbf{B}_h^{n+1} - 2\mathbf{B}_h^n + \mathbf{B}_h^{n-1}\|^2)\\
&\quad + \frac{1}{2}(|Q^{n+1}|^2 - |Q^n|^2 + |2Q^{n+1} - Q^n|^2 - |2Q^n - Q^{n-1}|^2\\
&\quad + |Q^{n+1} - 2Q^n + Q^{n-1}|^2)\\
&\quad + \frac{2\delta t^2}{3}\|\nabla p_h^{n+1}\|^2 - \frac{2\delta t^2}{3}\|\nabla p_h^n\|^2 + \frac{2\kappa\delta t^2}{3}\|\nabla r_h^{n+1}\|^2 - \frac{2\kappa\delta t^2}{3}\|\nabla r_h^n\|^2\\
&\quad + \frac{3}{2}\|\tilde{\mathbf{u}}_h^{n+1} - \mathbf{u}_h^{n+1}\|^2 + \frac{3\kappa}{2}\|\tilde{\mathbf{B}}_h^{n+1} - \mathbf{B}_h^{n+1}\|^2\\
&\quad = -2\nu\delta t\|\nabla\tilde{\mathbf{u}}_h^{n+1}\|^2 - 2\kappa\eta\delta t\|\mathrm{curl}\tilde{\mathbf{B}}_h^{n+1}\|^2.
\end{aligned}$$

After dropping several unnecessary positive terms, we arrive at (3.29) to finish the proof.

3.3. Decoupled implementation

In this subsection, we construct fully decoupled solution procedures for the proposed scheme (3.20)-(3.26) in which we make full use of the nonlocal property of the auxiliary variable Q. One can easily prove that the following fully decoupled linearized scheme is equivalent to the scheme (3.20)-(3.26), hence has the same stability and accuracy.

We split $\tilde{\mathbf{u}}_h^{n+1}, \tilde{\mathbf{B}}_h^{n+1}$ into a linear combination form in terms of Q^{n+1}, namely

$$\tilde{\mathbf{u}}_h^{n+1} = \tilde{\mathbf{u}}_{h1}^{n+1} + Q^{n+1}\tilde{\mathbf{u}}_{h2}^{n+1}, \quad \tilde{\mathbf{B}}_h^{n+1} = \tilde{\mathbf{B}}_{h1}^{n+1} + Q^{n+1}\tilde{\mathbf{B}}_{h2}^{n+1}, \tag{3.48}$$

where $\tilde{\mathbf{u}}_{h1}^{n+1}\in\mathbf{V}_h$, $\tilde{\mathbf{u}}_{h2}^{n+1}\in\mathbf{V}_h$, $\tilde{\mathbf{B}}_{h1}^{n+1}\in\mathbf{C}_h$, $\tilde{\mathbf{B}}_{h2}^{n+1}\in\mathbf{C}_h$.

Step 1: Using (3.48) and according to Q^{n+1}, we split (3.20) into the following two sub-equations:

$$\begin{cases}\frac{3}{2\delta t}(\tilde{\mathbf{u}}_{h1}^{n+1},\mathbf{v}_h)+\nu(\nabla\tilde{\mathbf{u}}_{h1}^{n+1},\nabla\mathbf{v}_h)=\frac{1}{2\delta t}(4\mathbf{u}_h^n-\mathbf{u}_h^{n-1},\mathbf{v}_h)-(\nabla p_h^n,\mathbf{v}_h),\\ \frac{3}{2\delta t}(\tilde{\mathbf{u}}_{h2}^{n+1},\mathbf{v}_h)+\nu(\nabla\tilde{\mathbf{u}}_{h2}^{n+1},\nabla\mathbf{v}_h)=-(\mathbf{u}_h^*\cdot\nabla)\mathbf{u}_h^*,\mathbf{v}_h)-\kappa(\mathbf{B}_h^*\times\text{curl}\mathbf{B}_h^*,\mathbf{v}_h).\end{cases}\tag{3.49}$$

It is very easy to solve the above two equations since they are linear elliptic equations with constant coefficients. The multigrid method [30] is very efficient for this type problem.

Step 2: Using (3.48) and according to Q^{n+1}, we split (3.21) into the following two sub-equations:

$$\begin{cases}\frac{3}{2\delta t}(\tilde{\mathbf{B}}_{h1}^{n+1},\mathbf{c}_h)+\eta(\text{curl}\tilde{\mathbf{B}}_{h1}^{n+1},\text{curl}\mathbf{c}_h)=\frac{1}{2\delta t}(4\mathbf{B}_h^n-\mathbf{B}_h^{n-1},\mathbf{c}_h)-(\nabla r_h^n,\mathbf{c}_h),\\ \frac{3}{2\delta t}(\tilde{\mathbf{B}}_{h2}^{n+1},\mathbf{c}_h)+\eta(\text{curl}\tilde{\mathbf{B}}_{h2}^{n+1},\text{curl}\mathbf{c}_h)=(\mathbf{u}_h^*\times\mathbf{B}_h^*,\text{curl}\mathbf{c}_h).\end{cases}\tag{3.50}$$

It is very easy to solve the above two equations by using the well-known fast solvers [31].

Step 3: By using (3.48), we rewrite (3.22) as follows:

$$(\frac{3}{2\delta t}-\eta_2)Q^{n+1}=\eta_1+\frac{1}{2\delta t}(4Q^n-Q^{n-1}),\tag{3.51}$$

where

$$\eta_i=\int_\Omega(\mathbf{u}_h^*\cdot\nabla)\mathbf{u}_h^*\cdot\tilde{\mathbf{u}}_{hi}^{n+1}d\mathbf{x}+\kappa\int_\Omega\mathbf{B}_h^*\times\text{curl}\mathbf{B}_h^*\cdot\tilde{\mathbf{u}}_{hi}^{n+1}d\mathbf{x}-\kappa\int_\Omega(\mathbf{u}_h^*\times\mathbf{B}_h^*)\cdot\text{curl}\tilde{\mathbf{B}}_{hi}^{n+1}d\mathbf{x}.$$

It is very easy to solve (3.51) since all terms in η_1 and η_2 are already obtained from Step 1 and Step 2.

Step 4: Update $\tilde{\mathbf{u}}_h^{n+1}$ and $\tilde{\mathbf{B}}_h^{n+1}$ by (3.48); solve (3.23) for p_h^{n+1}; solve (3.25) for r_h^{n+1}; update $\mathbf{u}_h^{n+1}$ by (3.24); update $\mathbf{B}_h^{n+1}$ from (3.26). The solvability of (3.51) can be briefly showed by verifying $\frac{3}{2\delta t}-\eta_2\neq 0$. We take $\mathbf{v}_h=\tilde{\mathbf{u}}_{h2}^{n+1}$ in the second equation in (3.49) to deduce

$$\frac{3}{2\delta t}\|\tilde{\mathbf{u}}_{h2}^{n+1}\|^2+\nu\|\nabla\tilde{\mathbf{u}}_{h2}^{n+1}\|^2=-\int_\Omega(\mathbf{u}_h^*\cdot\nabla)\mathbf{u}_h^*\cdot\tilde{\mathbf{u}}_{h2}^{n+1}d\mathbf{x}-\kappa\int_\Omega\mathbf{B}_h^*\times\text{curl}\mathbf{B}_h^*\cdot\tilde{\mathbf{u}}_{h2}^{n+1}d\mathbf{x}.$$

We take $\mathbf{c}_h=\kappa\tilde{\mathbf{B}}_{h2}^{n+1}$ in the second equation of (3.50) to derive

$$\frac{3\kappa}{2\delta t}\|\tilde{\mathbf{B}}_{h2}^{n+1}\|^2+\kappa\eta\|\text{curl}\tilde{\mathbf{B}}_{h2}^{n+1}\|^2=\kappa\int_\Omega(\mathbf{u}_h^*\times\mathbf{B}_h^*)\cdot\text{curl}\tilde{\mathbf{B}}_{h2}^{n+1}d\mathbf{x}.$$

Summing up the above two obtained equations, we derive $-\eta_2\geq 0$, that implies the solvability of (3.51).

From the above-detailed implementation process, it can be seen that the calculations of all unknown variables are completely decoupled. At each time step, the total cost only includes the computations of several elliptic equations. The decoupling of all equations and the characteristic of having only constant coefficients lead to highly efficient practical calculations.

Remark 3.5. The nonlocal variable Q can also provide a practical criterion of the time step adaptivity, in addition to its roles of maintaining stability and decoupling unknowns. Generally speaking, when Q^{n+1} deviates from 1, the time step size δt needs to be refined to maintain the accuracy. On the other hand, when Q^{n+1} stays close to 1, the time step size δt could be relaxed. The detailed mechanism of variable time step size is an interesting future work.

Remark 3.6. The work in [17–20] considered the following MHD model:

$$\begin{cases}\mathbf{u}_t-\nu\Delta\mathbf{u}+(\mathbf{u}\cdot\nabla)\mathbf{u}+\nabla p-(\mathbf{B}\cdot\nabla)\mathbf{B}=\mathbf{0},\\ \text{div}\mathbf{u}=0,\\ \mathbf{B}_t-\eta\Delta\mathbf{B}+(\mathbf{u}\cdot\nabla)\mathbf{B}-(\mathbf{B}\cdot\nabla)\mathbf{u}+\nabla r=\mathbf{0},\\ \text{div}\mathbf{B}=0,\\ \mathbf{u}|_{\partial\Omega}=\mathbf{0},\ \ \mathbf{B}|_{\partial\Omega}=\mathbf{0}.\end{cases}\tag{3.52}$$

By defining “Elsässer” variables $\mathbf{v}=\mathbf{u}+\mathbf{B}$, $\mathbf{w}=\mathbf{u}-\mathbf{B}$, $q=p+r$, $\lambda=p-r$, the system becomes

$$\begin{cases} \mathbf{v}_t - \frac{\nu+\eta}{2}\Delta\mathbf{v} - \frac{\nu-\eta}{2}\Delta\mathbf{w} + (\mathbf{w}\cdot\nabla)\mathbf{v} + \nabla q = \mathbf{0}, \\ \mathrm{div}\mathbf{v} = 0, \\ \mathbf{w}_t - \frac{\nu+\eta}{2}\Delta\mathbf{w} - \frac{\nu-\eta}{2}\Delta\mathbf{v} + (\mathbf{v}\cdot\nabla)\mathbf{w} + \nabla\lambda = \mathbf{0}, \\ \mathrm{div}\mathbf{w} = 0, \\ \mathbf{v}|_{\partial\Omega} = \mathbf{0}, \quad \mathbf{w}|_{\partial\Omega} = \mathbf{0}. \end{cases}$$

A significant merit of this formulation is that the two nonlinear terms $(\mathbf{w}\cdot\nabla)\mathbf{v}$ and $(\mathbf{v}\cdot\nabla)\mathbf{w}$ possess a skew-symmetric structure, i.e., $((\mathbf{w}\cdot\nabla)\mathbf{v},\mathbf{v}) = 0$, $((\mathbf{v}\cdot\nabla)\mathbf{w},\mathbf{w}) = 0$. By treating the two nonlinear terms as $(\mathbf{w}^*\cdot\nabla)\mathbf{v}^{n+1}$ and $(\mathbf{v}^*\cdot\nabla)\mathbf{w}^{n+1}$, in [18,19], a second-order time-accurate, decoupled, and stable scheme is developed under the condition of $\frac{1}{2} < \frac{\nu}{\eta} < 2$. The work in [18] extends this result and shows that the second-order scheme could be stable without the restriction on $\frac{\nu}{\eta}$ if a time step restriction of $\delta t < O(h^2)$ is satisfied. Meanwhile, from the identity $\mathbf{B}\times\mathrm{curl}\mathbf{B} = \nabla(\frac{1}{2}|\mathbf{B}|^2) - \mathbf{B}\cdot\nabla\mathbf{B}$, it can be seen that the term $\nabla(\frac{1}{2}|\mathbf{B}|^2)$ is not considered in (3.52). If one recovers the term $\nabla(\frac{1}{2}|\mathbf{B}|^2)$ in the model, the Elsässer variable method may not maintain the skew-symmetric structure of the nonlinear terms.

The major differences between this paper and the above works are the full MHD equations (2.11)-(2.14) and no restriction at all for the unconditional stability, based on the novel “zero-energy-contribution” feature.

Remark 3.7. The decoupling technique through the nonlocal variable Q is also suitable to deal with the so-called H^1 discretization incompressible MHD system [7] (or called penalty MHD equations), that reads as:

$$\begin{cases} \mathbf{u}_t - \nu\Delta\mathbf{u} + (\mathbf{u}\cdot\nabla)\mathbf{u} + \nabla p + \kappa\mathbf{B}\times\mathrm{curl}\mathbf{B} = \mathbf{0}, \\ \mathrm{div}\mathbf{u} = 0, \\ \mathbf{B}_t + \eta\,\mathrm{curl}\mathrm{curl}\mathbf{B} - \eta\nabla\mathrm{div}\mathbf{B} - \mathrm{curl}(\mathbf{u}\times\mathbf{B}) = \mathbf{0}, \\ \mathrm{div}\mathbf{B} = 0. \end{cases} \tag{3.53}$$

Note the coupling nonlinear terms are still the advection and Lorentz force, it can be formulated to the following equivalent form using Q:

$$\begin{cases} \mathbf{u}_t - \nu\Delta\mathbf{u} + Q(\mathbf{u}\cdot\nabla)\mathbf{u} + \nabla p + \kappa Q\mathbf{B}\times\mathrm{curl}\mathbf{B} = \mathbf{0}, \\ \mathrm{div}\mathbf{u} = 0, \\ \mathbf{B}_t + \eta\,\mathrm{curl}\mathrm{curl}\mathbf{B} - \eta\nabla\mathrm{div}\mathbf{B} - Q\,\mathrm{curl}(\mathbf{u}\times\mathbf{B}) = \mathbf{0}, \\ \mathrm{div}\mathbf{B} = 0, \\ Q_t = \int_\Omega(\mathbf{u}\cdot\nabla)\mathbf{u}\cdot\mathbf{u}d\mathbf{x} + \kappa\int_\Omega \mathbf{B}\times\mathrm{curl}\mathbf{B}\cdot\mathbf{u}d\mathbf{x} - \kappa\int_\Omega \mathbf{u}\times\mathbf{B}\cdot\mathrm{curl}\mathbf{B}d\mathbf{x}. \end{cases}$$

Using similar discretization methods and finite element space, one can easily construct a linear, decoupled, second-order time accurate, and unconditionally energy stable scheme for the above model. We leave the detailed procedure to the interested readers.

Remark 3.8. The nonhomogeneous boundary conditions $\mathbf{u}|_{\partial\Omega} = \mathbf{u}_b$, $\mathbf{B}\times\mathbf{n}|_{\partial\Omega} = \mathbf{B}_b$ instead of (2.15) can be handled with the same idea. We only need to slightly modify the nonlocal variable $Q(t)$ to include the boundary integration as follows:

$$\begin{cases} Q_t = \int\limits_\Omega (\mathbf{u}\cdot\nabla)\mathbf{u}\cdot\mathbf{u}d\mathbf{x} - \frac{1}{2}\int\limits_{\partial\Omega}(\mathbf{u}_b\cdot\mathbf{n})|\mathbf{u}_b|^2 ds + \kappa\int\limits_\Omega \mathbf{B}\times\mathrm{curl}\mathbf{B}\cdot\mathbf{u}d\mathbf{x} - \kappa\int\limits_\Omega \mathbf{u}\times\mathbf{B}\cdot\mathrm{curl}\mathbf{B}d\mathbf{x}, \\ Q|_{t=0} = 1. \end{cases}$$

By taking integration by parts, we can deduce $Q \equiv 1$ as well. In the decoupled procedures **Step 1** (3.49) and **Step 2** (3.50), we need to impose the boundary conditions $\tilde{\mathbf{u}}_{h1}^{n+1}|_{\partial\Omega} = \mathbf{u}_b^h$, $\tilde{\mathbf{u}}_{h2}^{n+1}|_{\partial\Omega} = \mathbf{0}$, $\tilde{\mathbf{B}}_{h1}^{n+1}\times\mathbf{n}|_{\partial\Omega} = \mathbf{B}_b^h$ and $\tilde{\mathbf{B}}_{h2}^{n+1}\times\mathbf{n}|_{\partial\Omega} = \mathbf{0}$, where the $\mathbf{u}_b^h$ and $\mathbf{B}_b^h$ are proper interpolations or projections of $\mathbf{u}_b$ and $\mathbf{B}_b$ in finite element spaces.

4. Numerical simulations

In this section, we present ample numerical simulations to show the stability and accuracy of the developed scheme (3.20)-(3.26) (abbreviated as DS, for short). We use Taylor-Hood elements for $\mathbf{V}_h$ and M_h (second-order polynomial $\mathcal{P}_2$ element for $\mathbf{V}_h$, linear polynomial $\mathcal{P}_1$ element for M_h) that satisfy the inf-sup condition (3.18) [39]. We also use the first family second-order $H(\mathrm{curl})$-conforming Nédélec edge $\mathcal{N}_2$ element [40,41] for $\mathbf{C}_h$, second-order polynomial $\mathcal{P}_2$ element for S_h, which also satisfy the inf-sup condition (3.19) since $\nabla S_h \subset \mathbf{C}_h$.

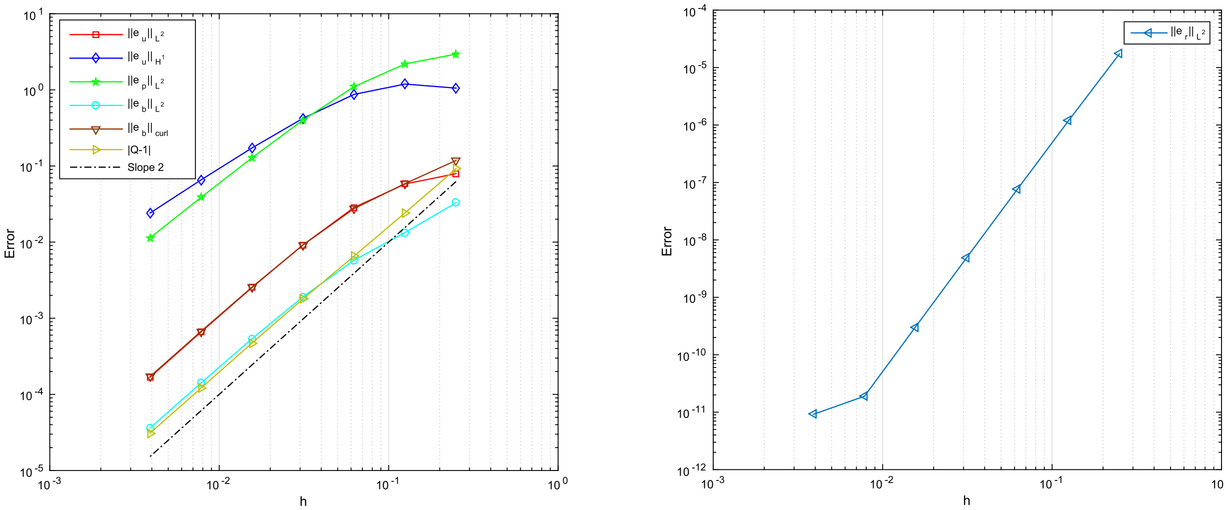

(a) Errors and convergence orders of $h = \delta t$.

(b) Errors of r of $h = \delta t$.

Fig. 1. The numerical errors of $\|e_u\|_{L^2}$, $\|e_u\|_{H^1}$, $\|e_p\|_{L^2}$, $\|e_b\|_{L^2}$, $\|e_b\|_{\text{curl}}$, $|Q-1|$, and r at $t = 1$ that are computed by using $h = \delta t$ with the given exact solutions (4.1).

Table 1
The numerical errors and convergence orders for $\|e_u\|_{H^1}$ and $\|e_p\|_{L^2}$ in an interior domain $(0.1, 0.9)^2$ at $t = 1$ that are computed using $\delta t = h$ with the exact solutions of (4.1).

h	δt	$\|e_u\|_{H^1}$	Order	$\|e_p\|_{L^2}$	Order
$\frac{1}{4}$	$\frac{1}{4}$	1.06629	–	1.47116	–
$\frac{1}{8}$	$\frac{1}{8}$	0.965592	0.14	1.01415	0.54
$\frac{1}{16}$	$\frac{1}{16}$	0.262053	1.88	0.415646	1.29
$\frac{1}{32}$	$\frac{1}{32}$	0.0608671	2.10	0.113079	1.88
$\frac{1}{64}$	$\frac{1}{64}$	0.0163281	1.90	0.0299588	1.92
$\frac{1}{128}$	$\frac{1}{128}$	0.00418888	1.96	0.00771162	1.96
$\frac{1}{256}$	$\frac{1}{256}$	0.00105864	1.98	0.00194857	1.98

4.1. Accuracy test

We verify the convergence order of the scheme DS in this example. We set the exact solution (4.1) to verify the temporal-spatial accuracy. We use the computational domain $(0, 1)^2$ and set parameters $R_e = R_m = \kappa = 1$. The source terms and boundary conditions are chosen such that the exact solution are given as

$$\begin{cases} \mathbf{u} = (\exp(t)\cos(y), \exp(t)\sin(x)), \quad p = 10t^2(2x-1)(2y-1), \\ \mathbf{B} = (\sin(t+y), \cos(t+x)), \quad r = 0. \end{cases} \tag{4.1}$$

In this case, we set $h = \delta t$, and refine h and δt simultaneously by $h = \delta t = \frac{1}{2^i}$, $i = 2, 3, \cdots, 8$.

In Fig. 1(a), the L^2 errors of $\mathbf{u}$, $\mathbf{B}$, $H(\text{curl})$ error of $\mathbf{B}$, and $|Q-1|$ at $t = 1$ are plotted, which show the second-order accuracy. However, the L^2 error of p and H^1 error of $\mathbf{u}$ are not full second-order accuracy due to a numerical boundary layer [43]. If the L^2 error of p and H^1 error of $\mathbf{u}$ are measured in an interior domain $(0.1, 0.9)^2$, they all reach the second-order accuracy, see Table 1. Fig. 1(b) illustrates the numerical solution of r is very close to zero with the mesh refining.

4.2. Energy stability test

In this example, we verify the energy stability of the scheme DS. We choose the computed domain to be $\Omega = (0, 1)^2$, and load the following initial conditions of $\mathbf{u}$, p, $\mathbf{B}$, and r,

$$\begin{cases} \mathbf{u}^0 = \Big(x^2(x-1)^2 y(y-1)(2y-1), \; -y^2(y-1)^2 x(x-1)(2x-1)\Big), \; p^0 = 0, \\ \mathbf{B}^0 = \Big(\sin^2(\pi x)\sin(\pi y)\cos(\pi y), -\sin^2(\pi y)\cos(\pi x)\sin(\pi x)\Big), \; r^0 = 0. \end{cases} \tag{4.2}$$

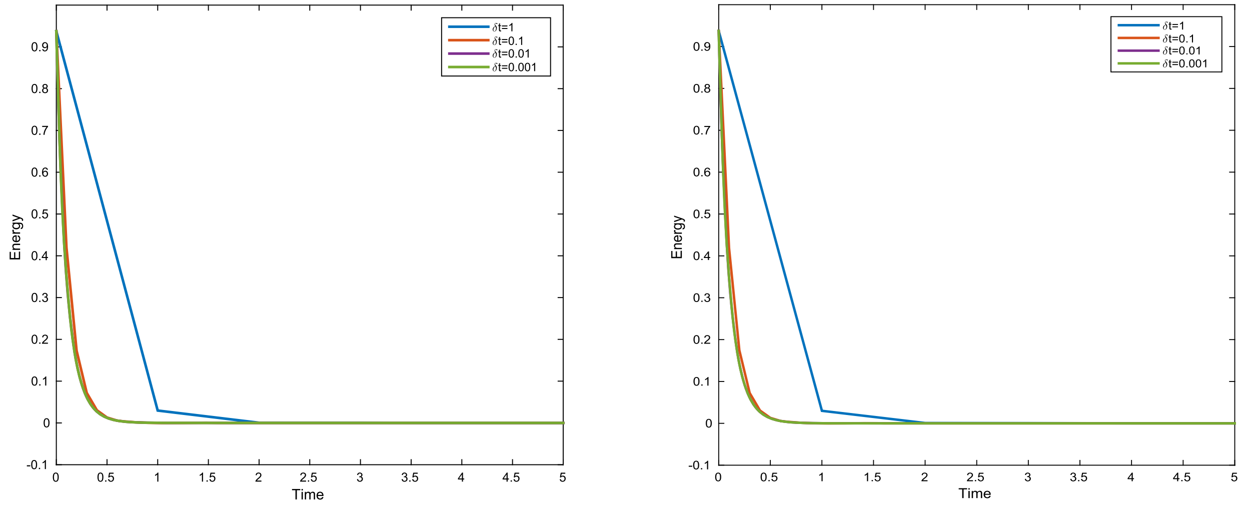

(a) DS

(b) Imp-Exp.

Fig. 2. Time evolution of the free energy functional for four different time step sizes with $R_e = R_m = \kappa = 10$ computed by (a) DS and (b) Imp-Exp. (For interpretation of the colors in the figure(s), the reader is referred to the web version of this article.)

For comparison, we also test the stability performance with the following second-order implicit-explicit (abbreviated as Imp-Exp) scheme (4.3) that reads as,

$$\begin{cases} \left(\dfrac{3\mathbf{u}_h^{n+1} - 4\mathbf{u}_h^n + \mathbf{u}_h^{n-1}}{2\delta t}, \mathbf{v}_h\right) + \nu(\nabla \mathbf{u}_h^{n+1}, \nabla \mathbf{v}_h) + ((\mathbf{u}_h^* \cdot \nabla)\mathbf{u}_h^*, \mathbf{v}_h) \\ \qquad\qquad - (p_h^{n+1}, \mathrm{div}\mathbf{v}_h) + \kappa(\mathbf{B}_h^* \times \mathrm{curl}\mathbf{B}_h^*, \mathbf{v}_h) + (\mathrm{div}\mathbf{u}_h^{n+1}, q_h) = 0, \\ \left(\dfrac{3\mathbf{B}_h^{n+1} - 4\mathbf{B}_h^n + \mathbf{B}_h^{n-1}}{2\delta t}, \mathbf{c}_h\right) + \eta(\mathrm{curl}\mathbf{B}_h^{n+1}, \mathrm{curl}\mathbf{c}_h) - (\mathbf{u}_h^* \times \mathbf{B}_h^*, \mathrm{curl}\mathbf{c}_h) \\ \qquad\qquad + (\nabla r_h^{n+1}, \mathbf{c}_h) + (\mathbf{B}_h^{n+1}, \nabla s_h) = 0, \end{cases} \tag{4.3}$$

where all nonlinear terms are treated explicitly while the linear terms are treated implicitly.

We fix the mesh size $h = \frac{1}{16}$, and adopt two sets of physical parameter $R_e = R_m = \kappa = 10$ (low stiffness) and $R_e = R_m = \kappa = 100$ (high stiffness). We vary time step size $\delta t = 1.0$, 0.1, 0.01, and 0.001 and compare the total free energy $E(\mathbf{u}^n, \mathbf{B}^n) = \frac{1}{2}\|\mathbf{u}^n\|^2 + \frac{1}{2}\kappa\|\mathbf{B}^n\|^2$ computed by the our scheme DS and the scheme Imp-Exp.

In Fig. 2, for $R_e = R_m = \kappa = 10$, we observe that all energy curves computed by both schemes show monotonic decays for all time step sizes. This means for low Reynolds number (low stiffness case), both schemes are energy stable.

In Fig. 3, for $R_e = R_m = \kappa = 100$, we can see that the scheme Imp-Exp is not stable when adopting large time steps $\delta t \geq 0.01$, which shows that the scheme (4.3) is only conditionally energy stable. While all energy curves computed by DS always show monotonic decays, thereby verifying its unconditional energy stability.

4.3. Island coalescence

We consider a driven magnetic reconnection example, the so-called island coalescence problem. Fast magnetic reconnection is a long-standing issue for understanding plasma physics. The island coalescence problem presents two magnetic islands embedded in a Harris current sheet by setting a perturbed Harris sheet magnetic field configuration as initial conditions. The combined magnetic field produced by the two magnetic islands produces Lorentz forces, which pull the islands together over time. Concerning the physical background of this problem and the extensive numerical simulations for it, we refer to [44–49].

In this simulation, we set the computational domain as $\Omega = [-1, 1] \times [-0.5, 0.5]$, and other model parameters as $R_e = R_m = 1000$, $\kappa = 1.0$. We equip a source term $\mathbf{g}$ for magnetic equation (2.13), where

$$\mathbf{g} = \left(\frac{2\zeta(1-\varepsilon^2)}{\delta^2}\frac{\sinh(\frac{y}{\delta})}{(\cosh(\frac{y}{\delta}) + \varepsilon\cos(\frac{x}{\delta}))^3}, \frac{2\varepsilon\zeta(1-\varepsilon^2)}{\delta^2}\frac{\sin(\frac{x}{\delta})}{(\cosh(\frac{y}{\delta}) + \varepsilon\cos(\frac{x}{\delta}))^3}\right). \tag{4.4}$$

The initial conditions are set as

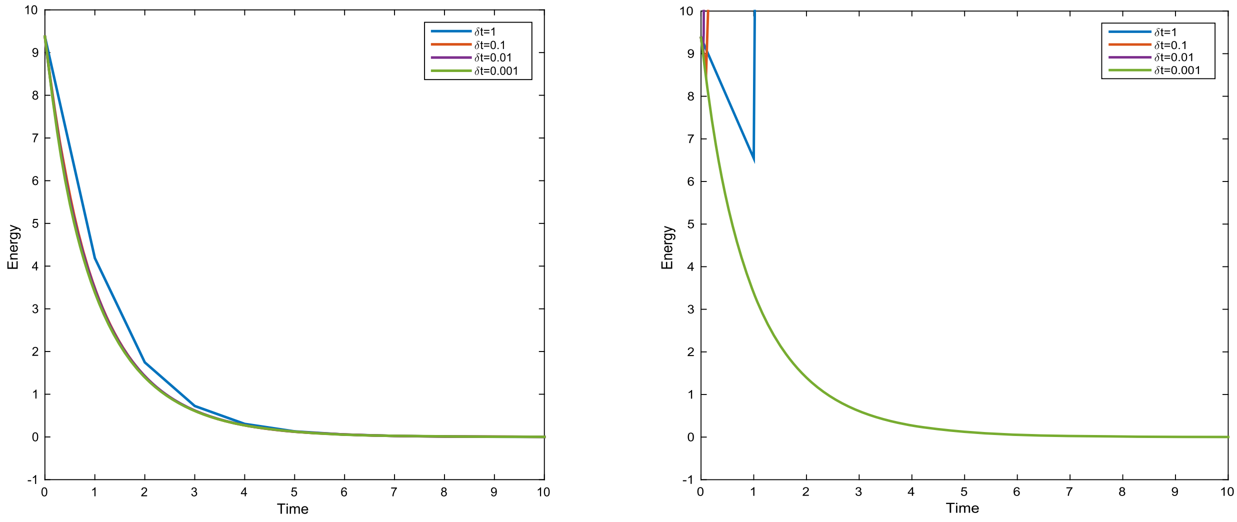

(a) DS.

(b) Imp-Exp.

Fig. 3. Time evolution of the free energy functional for four different time step sizes with $R_e = R_m = \kappa = 100$ computed by (a) DS and (b) Imp-Exp.

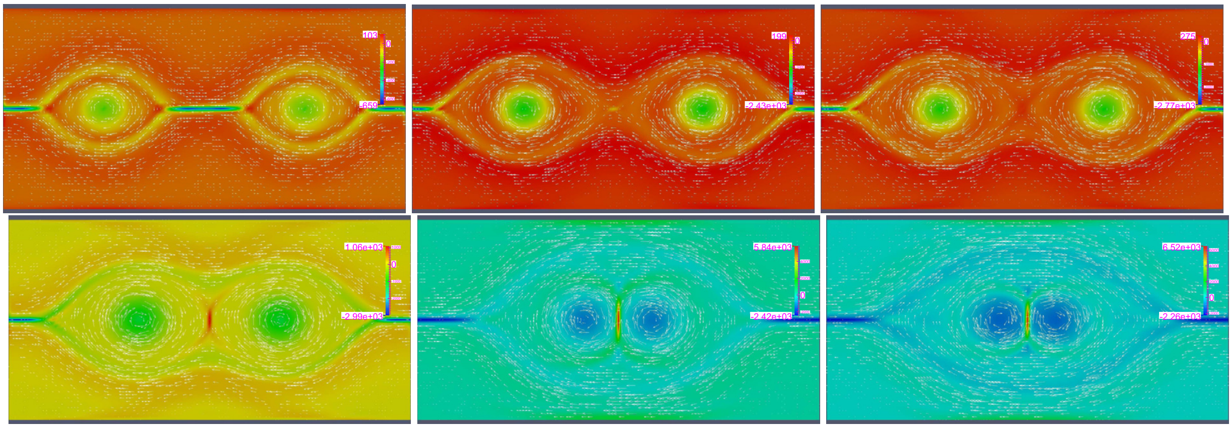

Fig. 4. Snapshots of the magnetic field **B** (in arrows) and the magnitude of the current density J (in colormap) at $t = 0.2, 1.3, 1.4, 1.5, 2, 2.2$.

$$\mathbf{u}_0 = (0, 0),\ \mathbf{B}_0 = \left(\frac{\sinh(\frac{y}{\delta})}{\cosh(\frac{y}{\delta}) + \varepsilon\cos(\frac{x}{\delta})} + \delta_1,\ \frac{\varepsilon\sin(\frac{x}{\delta})}{\cosh(\frac{y}{\delta}) + \varepsilon\cos(\frac{x}{\delta})} + \delta_2 \right), \tag{4.5}$$

where $\delta_1 = -\frac{\gamma}{\pi}\cos(\pi x)\sin(\frac{1}{2}\pi y)$, $\delta_2 = \frac{\gamma}{2\pi}\cos(\frac{1}{2}\pi y)\sin(\pi x)$ are perturbations, $\zeta = 1.0$, $\varepsilon = 0.2$, $\delta = \frac{1}{2\pi}$, and $\gamma = -0.01$. The boundary conditions are zero tangential stress ($\mathbf{u} = 0$) and perfect conducting wall ($\mathbf{B} = 0$) on the top and bottom boundaries, and periodic conditions on the left and right walls.

We set the time step size $\delta t = \frac{1}{5000}$, and the spatial mesh size $h = \frac{1}{64}$. In Fig. 4, we plot the vector field of the magnetic field **B** and the magnitude of the current density J ($J = \mathrm{curl}\mathbf{B}$). We observe the dynamical reconnection behaviors of magnetic islands and current density during the coalescence process. At $t = 1.5$ s, the two islands start to coalesce, and a sharp peak in current density is produced where the magnetic field lines reconnect. In Fig. 5, we plot the magnitude of the pressure at different times, in which, the pressure also displays the coalescence process as the magnetic field **B**. In Fig. 6, we plot the velocity field **u** at different times.

4.4. Hydromagnetic Kelvin-Helmholtz instability

The Kelvin-Helmholtz (K-H) instability in sheared flow configurations is an efficient mechanism that cause fluid mixing, momentum and energy transfer, and turbulence development. These issues need to be considered when studying various space, celestial and geophysical conditions involving shear plasma flow. Related configurations include the interface between the solar wind and the magnetosphere, and the coronal belt that moves in the solar wind. Since most astrophysical envi-

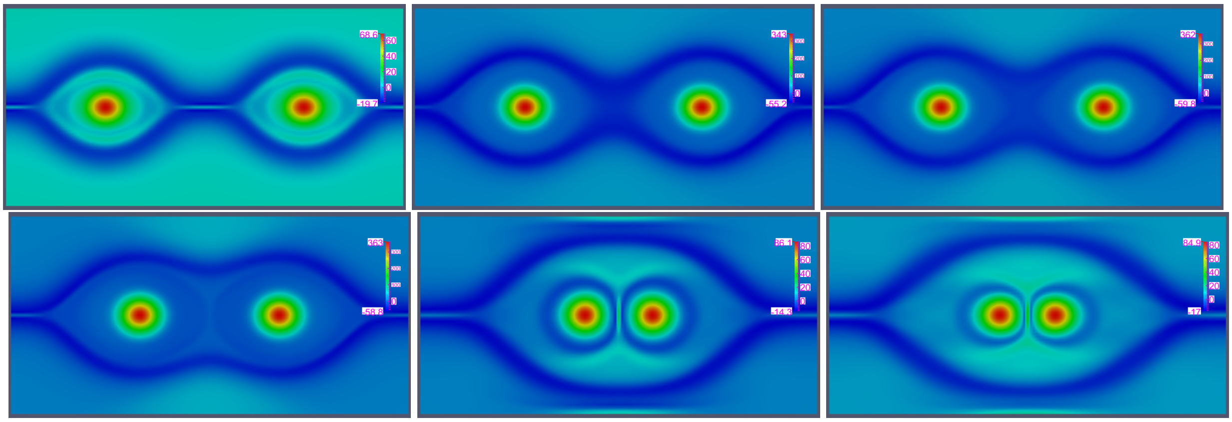

Fig. 5. Snapshots of the pressure p (in colormap) at $t = 0.2, 1.3, 1.4, 1.5, 2, 2.2$.

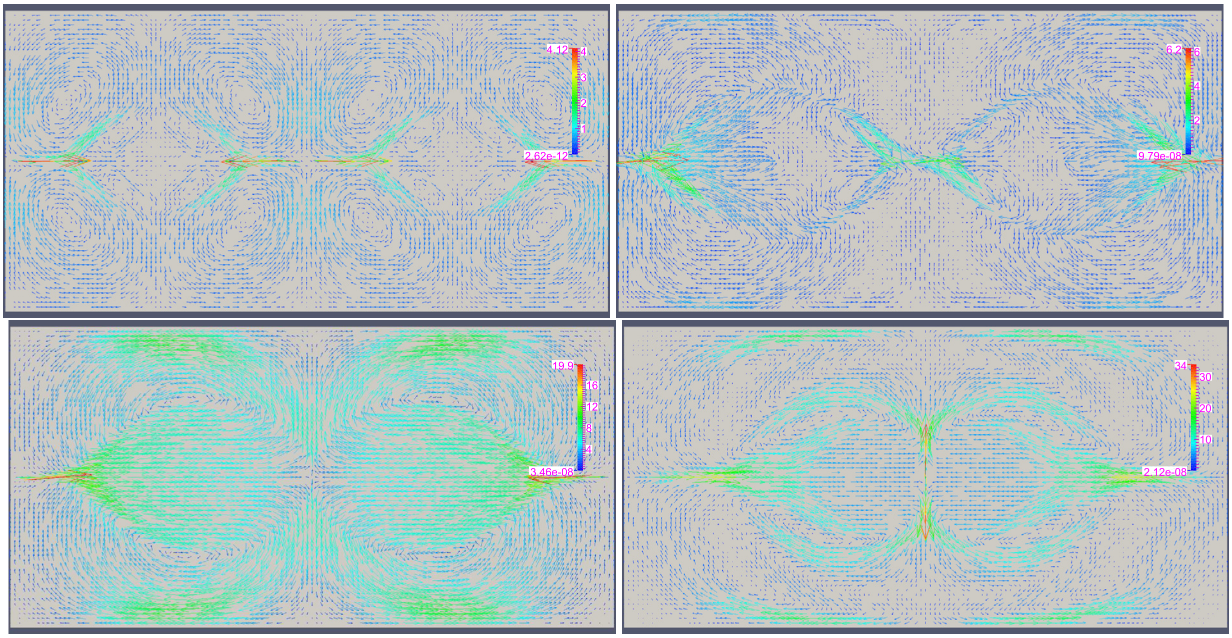

Fig. 6. Snapshots of the velocity field $\mathbf{u}$ at $t = 0.2, 1, 1.5, 2$.

ronments are electrically conductive, and related fluids are likely to be magnetized, it is important to understand the role of magnetic field in K-H instability [2,49,12,50–52].

We study occurrence of the K-H instability in a single shear flow configuration that is embedded in a uniform flow-aligned magnetic field. The simulation is performed in a computed domain of $\Omega = [0, 2] \times [0, 1]$. The initial velocity field is $\mathbf{u}_0 = (1.5, 0)$ in the top half domain, and $\mathbf{u}_0 = (-1.5, 0)$ in the bottom half domain. The sheared initial magnetic field is $\mathbf{B}_0 = (\tanh(y/\varepsilon), 0)$ where $\varepsilon = 0.07957747154595$ (cf. [49]). The velocity $\mathbf{u}$, magnetic field $\mathbf{B}$ are periodic boundary conditions on left and right boundaries. On the top and bottom boundaries, the second component $v = 0$ of the velocity field $\mathbf{u} = (u, v)$ is imposed. The boundary conditions for $\mathbf{B}$ are $\mathbf{B} \times \mathbf{n} = \mathbf{B}_0 \times \mathbf{n}$ for the top boundary and $\mathbf{B} \times \mathbf{n} = -\mathbf{B}_0 \times \mathbf{n}$ for the bottom. We set the model parameters as $R_e = 1000$, $R_m = 1000$, $\kappa = 0.095$, $h = \frac{1}{40}$, $\delta t = \frac{1}{400}$.

In Fig. 7, we show snapshots of the magnitude of B_x ($\mathbf{B} = (B_x, B_y)$) at various times that is superimposed by the velocity field $\mathbf{u}$. We observe that over time, the vortexes start to form at around $t = 3$. After $t = 3.5$, the profiles of vortexes and the magnetic field show the typical structure of K-H instability, and it deforms and rotates along with the flow soon. In Fig. 8, we plot the pressure p at various times, and we can see that the contours of p correspond with the B_x. The obtained numerical results coincide well with the numerical/experimental results in [51,50,52], qualitatively.

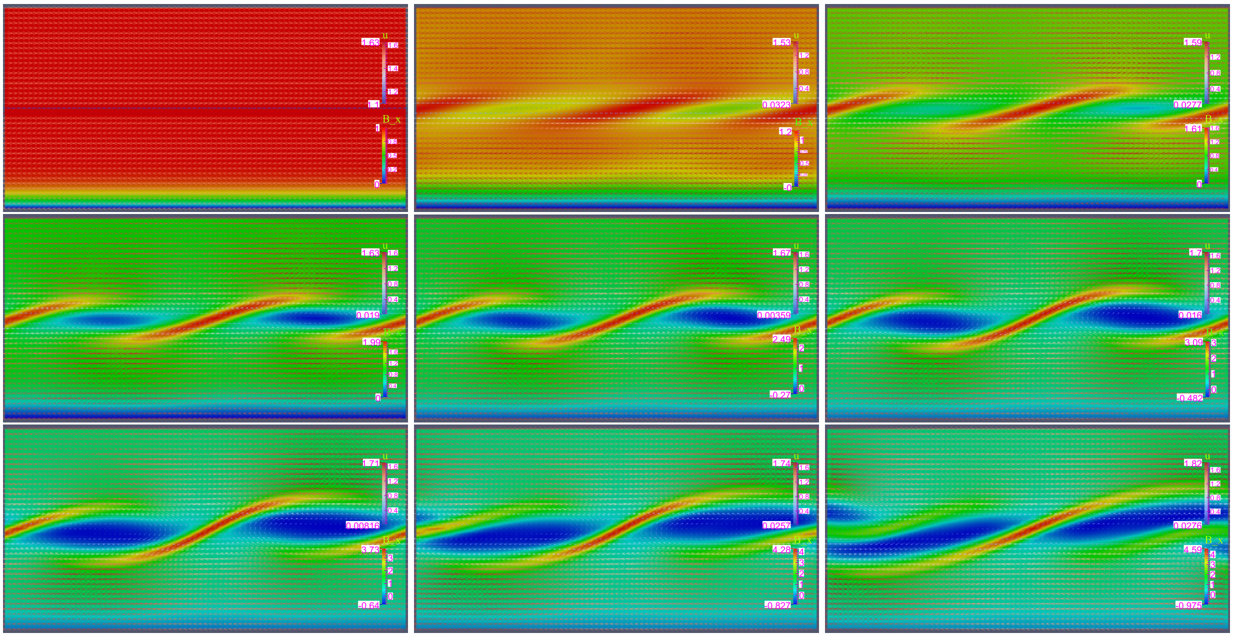

Fig. 7. The velocity field $\mathbf{u}$ with the filled contour of B_x that shows the hydromagnetic K-H instability. Snapshots are taken at $t = 0.01, 2.5, 3, 3.25, 3.5, 3.75, 4, 4.25, 4.5$.

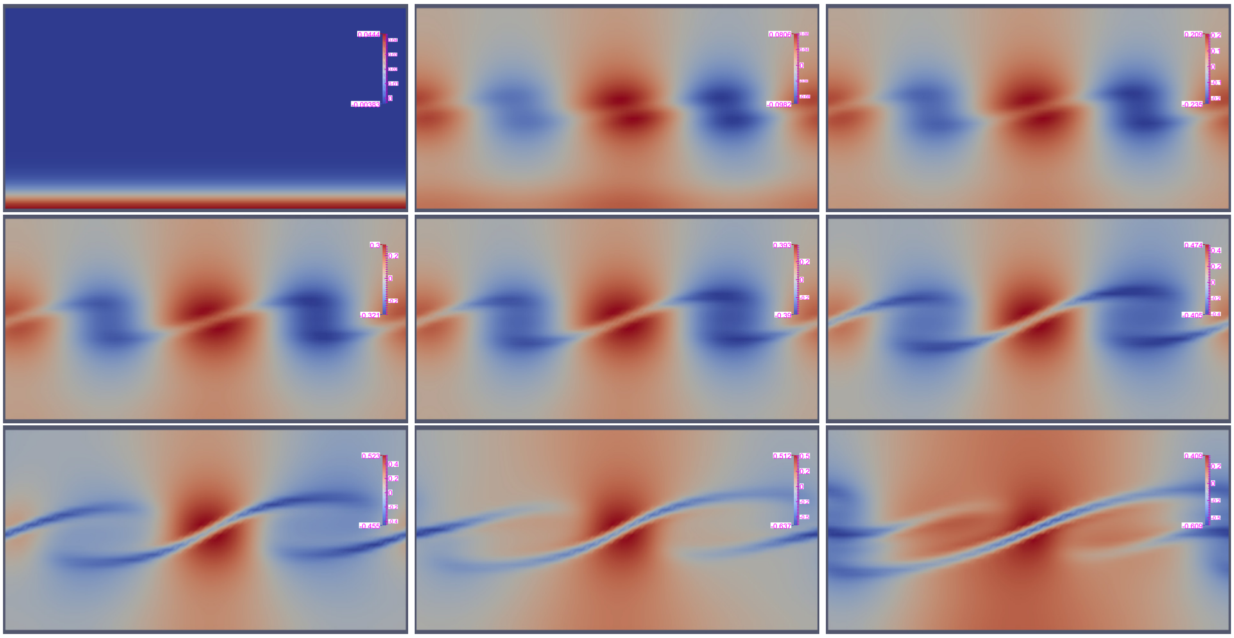

Fig. 8. Snapshots of the pressure p taken at $t = 0.01, 2.5, 3, 3.25, 3.5, 3.75, 4, 4.25, 4.5$.

4.5. 3D driven cavity flow

In this example, we simulate a benchmark problem of three-dimensional driven cavity flow, see [53,54,12].

We set the computational domain as $\Omega = [0, 1]^3$. The top boundary $(z = 1)$ condition are set by $\mathbf{u} = (1, 0, 0)$, no slip boundary conditions $(\mathbf{u} = \mathbf{0})$ are imposed on other walls. An external magnetic field effect is imposed by setting the magnetic field boundary of $\mathbf{B} \times \mathbf{n} = (-1, 0, 0) \times \mathbf{n}$ on the walls. The initial conditions are set as $\mathbf{u}(0, \mathbf{x}) = (u_x, 0, 0)$ where $u_x = 1$ for $z = 1$ and $u_x = 0$ for $z < 1$, $\mathbf{B}(0, \mathbf{x}) = (-1, 0, 0)$. We set model parameters as $R_e = 100, \kappa = 1, h = \frac{1}{12}, \delta t = \frac{1}{100}$.

In Fig. 9, we plot the two-dimensional cut-off planes of the streamlines of the velocity field at $y = 0.5$ for the magnetic Reynolds number $R_m = 0.1$, 1, and 10. We observe that for low magnetic Reynolds number, the solution of velocity is

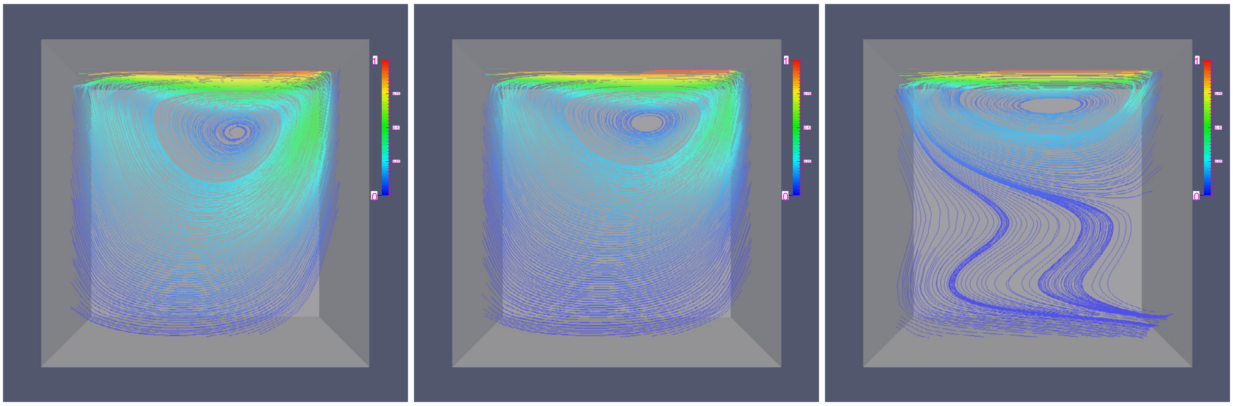

(a) $R_m = 0.1$. (b) $R_m = 1$. (c) $R_m = 10$.

Fig. 9. Streamlines of velocity at $y = 0.5$ for $R_e = 100$, $\kappa = 1$.

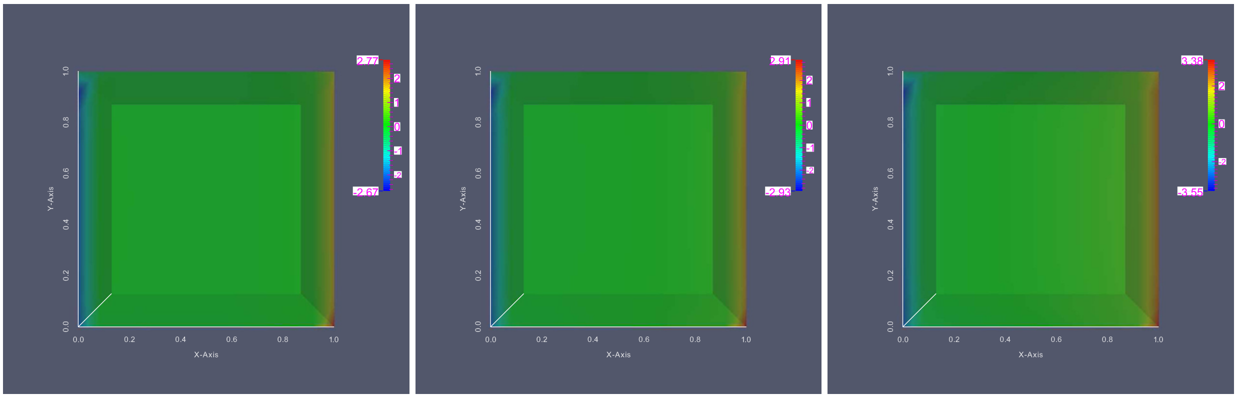

(a) $R_m = 0.1$. (b) $R_m = 1$. (c) $R_m = 10$.

Fig. 10. Pressure contours for $R_e = 100$, $\kappa = 1$ seen from top.

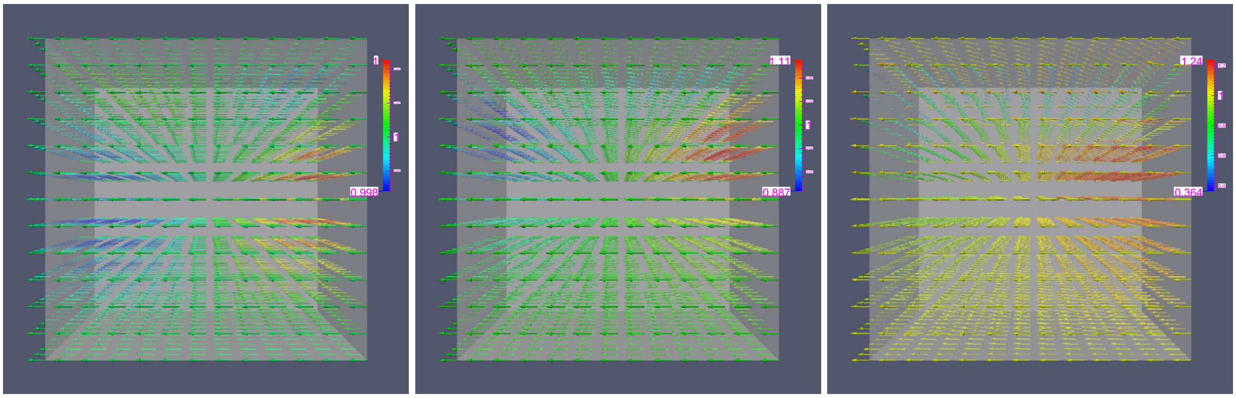

(a) $R_m = 0.1$. (b) $R_m = 1$. (c) $R_m = 10$.

Fig. 11. Vector field of magnetic field for $R_e = 100$, $\kappa = 1$.

dominated by one large vortex (shown in Fig. 9(a) and (b)). While as R_m increases, the vortex pushes upward in the domain, and the lower part velocity streamlines distort (shown in Fig. 9(c)). The obtained numerical simulations are very close to the results in the literatures [54,12]. In Fig. 10, we also demonstrate the magnitude of pressure contours, which indicate the pressure gradient mainly distribute over the two top corners in the cavity. The vector fields of the magnetic field are depicted in Fig. 11. We find the induced magnetic field is almost equal to the imposed magnetic field $(-1, 0, 0)$

for the small magnetic Reynolds number R_m (shown in Fig. 11(a)). With the increasing R_m, the induced magnetic field in the cavity gradually deviates the external imposed magnetic field because of the enhanced fluids convective action(shown in Fig. 11(c)).

5. Concluding remarks

We design a "desired" type of fully-discrete finite element scheme to solve the MHD system, namely, the scheme is fully-decoupled, linear, second-order time accurate, and unconditionally energy stable. The novelty of the developed scheme is that it utilizes the special characteristic of "zero-contribution-energy" satisfied by the advection and Lorentz force and design a special ODE based on it. The property is actually well-known, but never had been used in the design of numerical schemes. This property and the associated ODE based on it play a key role in obtaining the fully decoupled structure while maintaining the unconditional energy stability. The novel scheme is very efficient since it only needs to solve several independent linear elliptic sub-equations with constant coefficients and it can easily obtain second-order numerical solutions with unconditional energy stability. *To the best of the author's knowledge, for the MHD system, this is the first second-order scheme that can simultaneously have so many desirable properties*.

CRediT authorship contribution statement

Guo-Dong Zhang: Formal analysis, Funding acquisition, Methodology, Project administration, Software, Validation, Writing – original draft. **Xiaoming He:** Conceptualization, Formal analysis, Funding acquisition, Methodology, Project administration, Resources, Validation, Writing – review & editing. **Xiaofeng Yang:** Conceptualization, Formal analysis, Funding acquisition, Methodology, Project administration, Resources, Validation, Writing – review & editing.

Declaration of competing interest

The authors declare that they have no known competing financial interests or personal relationships that could have appeared to influence the work reported in this paper.

Acknowledgements

G.-D. Zhang's work was partially supported by National Natural Science Foundation of China under grant numbers 11771375 and 12171415. X. He's work was partially supported by National Science Foundation under grant number DMS-1818642. X. Yang's work was partially supported by National Science Foundation under grant numbers DMS-1818783 and DMS-2012490.

References

[1] R.J. Moreau, Magnetohydrodynamics, vol. 3, Springer Science & Business Media, 2013.
[2] J.P. Goedbloed, R. Keppens, S. Poedts, Advanced Magnetohydrodynamics: With Applications to Laboratory and Astrophysical Plasmas, Cambridge University Press, 2010.
[3] E.R. Priest, A.W. Hood, Advances in Solar System Magnetohydrodynamics, Cambridge University Press, 1991.
[4] Y. He, Unconditional convergence of the Euler semi-implicit scheme for the three-dimensional incompressible MHD equations, IMA J. Numer. Anal. 35 (2) (2014) 767–801.
[5] K. Wu, Positivity-preserving analysis of numerical schemes for ideal magnetohydrodynamics, SIAM J. Numer. Anal. 56 (4) (2018) 2124–2147.
[6] W. Layton, H. Tran, C. Trenchea, Numerical analysis of two partitioned methods for uncoupling evolutionary MHD flows, Numer. Methods Partial Differ. Equ. 30 (4) (2014) 1083–1102.
[7] M.D. Gunzburger, A.J. Meir, J.S. Peterson, On the existence, uniqueness, and finite element approximation of solutions of the equations of stationary, incompressible magnetohydrodynamics, Math. Comput. 56 (194) (1991) 523–563.
[8] K. Wu, D. Xiu, X. Zhong, A WENO-based stochastic Galerkin scheme for ideal MHD equations with random inputs, Commun. Comput. Phys. 30 (2) (2021) 423–447.
[9] N.B. Salah, A. Soulaimani, W.G. Habashi, A finite element method for magnetohydrodynamics, Comput. Methods Appl. Mech. Eng. 190 (43) (2001) 5867–5892.
[10] J.H. Adler, T.R. Benson, E.C. Cyr, S.P. MacLachlan, R.S. Tuminaro, Monolithic multigrid methods for two-dimensional resistive magnetohydrodynamics, SIAM J. Sci. Comput. 38 (1) (2016) B1–B24.
[11] J.-F. Gerbeau, C. Le Bris, T. Lelièvre, Mathematical Methods for the Magnetohydrodynamics of Liquid Metals, Clarendon Press, 2006.
[12] E.G. Phillips, J.N. Shadid, E.C. Cyr, H.C. Elman, R.P. Pawlowski, Block preconditioners for stable mixed nodal and edge finite element representations of incompressible resistive MHD, SIAM J. Sci. Comput. 38 (6) (2016) B1009–B1031.
[13] S. Badia, R. Planas, J.V. Gutiérrez-Santacreu, Unconditionally stable operator splitting algorithms for the incompressible magnetohydrodynamics system discretized by a stabilized finite element formulation based on projections, Int. J. Numer. Methods Eng. 93 (3) (2013) 302–328.
[14] J. Yang, S. Mao, X. He, X. Yang, Y. He, A diffuse interface model and semi-implicit energy stable finite element method for two-phase magnetohydrodynamic flows, Comput. Methods Appl. Mech. Eng. 356 (2019) 435–464.
[15] S. Mabuza, J.N. Shadid, E.C. Cyr, R.P. Pawlowski, D. Kuzmin, A linearity preserving nodal variation limiting algorithm for continuous Galerkin discretization of ideal MHD equations, J. Comput. Phys. 410 (2020) 109390.
[16] Y. Rong, Y. Hou, A partitioned second-order method for magnetohydrodynamic flows at small magnetic Reynolds numbers, Numer. Methods Partial Differ. Equ. 33 (6) (2017) 1966–1986.
[17] C. Trenchea, Unconditional stability of a partitioned imex method for magnetohydrodynamic flows, Appl. Math. Lett. 27 (2014) 97–100.

[18] T. Heister, M. Mohebujjaman, L.G. Rebholz, Decoupled, unconditionally stable, higher order discretizations for MHD flow simulation, J. Sci. Comput. 71 (1) (2017) 21–43.
[19] Y. Li, C. Trenchea, Partitioned second order method for magnetohydrodynamics in Elsässer variables, Discrete Contin. Dyn. Syst., Ser. B 23 (7) (2018) 2803.
[20] M. Akbas, S. Kaya, M. Mohebujjaman, L. Rebholz, Numerical analysis and testing of a fully discrete, decoupled penalty-projection algorithm for MHD in Elsässer variable, Int. J. Numer. Anal. Model. 13 (1) (2016) 90–113.
[21] G.-D. Zhang, Y. He, Decoupled schemes for unsteady MHD equations II: Finite element spatial discretization and numerical implementation, Comput. Math. Appl. (2015) 395–414.
[22] G.-D. Zhang, Y. He, Decoupled schemes for unsteady MHD equations. I. Time discretization, Numer. Methods Partial Differ. Equ. 33 (3) (2017) 956–973.
[23] Q. Zhang, H. Su, X. Feng, A partitioned finite element scheme based on gauge-Uzawa method for time-dependent MHD equations, Numer. Algorithms 78 (1) (2018) 277–295.
[24] H. Choi, J. Shen, Efficient splitting schemes for magneto-hydrodynamic equations, Sci. China Math. 59 (8) (2016) 1495–1510.
[25] X. Yang, G.-D. Zhang, X. He, Convergence analysis of an unconditionally energy stable projection scheme for magneto-hydrodynamic equations, Appl. Numer. Math. 136 (2019) 235–256.
[26] F. Bai, D. Han, X. He, X. Yang, Deformation and coalescence of ferrodroplets in Rosensweig model using the phase field and modified level set approaches under uniform magnetic fields, Commun. Nonlinear Sci. Numer. Simul. 85 (2020) 105213.
[27] G. Zhang, X. He, X. Yang, Decoupled, linear, and unconditionally energy stable fully-discrete finite element numerical scheme for a two-phase ferrohydrodynamics model, SIAM J. Sci. Comput. 43 (1) (2021) B167–B193.
[28] G.-D. Zhang, X. He, X. Yang, Fully decoupled, linear and unconditionally energy stable time discretization scheme for solving the magneto-hydrodynamic equations, J. Comput. Appl. Math. 369 (2020) 112636.
[29] G.-D. Zhang, X. He, X. Yang, A decoupled, linear and unconditionally energy stable scheme with finite element discretizations for magneto-hydrodynamic equations, J. Sci. Comput. 81 (3) (2019) 1678–1711.
[30] J. Xu, Iterative methods by space decomposition and subspace correction, SIAM Rev. 34 (4) (1992) 581–613.
[31] R. Hiptmair, J. Xu, Nodal auxiliary space preconditioning in H (curl) and H (div) spaces, SIAM J. Numer. Anal. 45 (6) (2007) 2483–2509.
[32] X. Yang, On a novel fully-decoupled, second-order accurate energy stable numerical scheme for a binary fluid-surfactant phase-field model, SIAM J. Sci. Comput. 43 (2021) B479–B507.
[33] X. Yang, Numerical approximations of the Navier-Stokes equation coupled with volume-conserved multi-phase-field vesicles system: fully-decoupled, linear, unconditionally energy stable and second-order time-accurate numerical scheme, Comput. Methods Appl. Mech. Eng. 375 (2021) 113600.
[34] X. Yang, A new efficient fully-decoupled and second-order time-accurate scheme for Cahn-Hilliard phase-field model of three-phase incompressible flow, Comput. Methods Appl. Mech. Eng. 376 (2021) 13589.
[35] X. Yang, A novel fully-decoupled, second-order time-accurate, unconditionally energy stable scheme for a flow-coupled volume-conserved phase-field elastic bending energy model, J. Comput. Phys. 432 (2021) 110015.
[36] X. Yang, A novel fully decoupled scheme with second-order time accuracy and unconditional energy stability for the Navier-Stokes equations coupled with mass-conserved Allen-Cahn phase-field model of two-phase incompressible flow, Int. J. Numer. Methods Eng. 122 (5) (2021) 1283–1306.
[37] X. Yang, A novel fully-decoupled, second-order and energy stable numerical scheme of the conserved Allen-Cahn type flow-coupled binary surfactant model, Comput. Methods Appl. Mech. Eng. 373 (2021) 113502.
[38] D. Schötzau, Mixed finite element methods for stationary incompressible magneto–hydrodynamics, Numer. Math. 96 (4) (2004) 771–800.
[39] V. Girault, P. Raviart, Finite Element Method for Navier-Stokes Equations: Theory and Algorithms, Springer-Verlag, Berlin, Heidelberg, 1987, pp. 395–414.
[40] J.C. Nédélec, A new family of mixed finite elements in R^3, Numer. Math. 50 (1) (1986) 57–81.
[41] P. Monk, Finite Element Methods for Maxwell's Equations, Oxford University Press, 2003.
[42] J.L. Guermond, P. Minev, J. Shen, An overview of projection methods for incompressible flows, Comput. Methods Appl. Mech. Eng. 195 (2006) 6011–6045.
[43] W. E, J.G. Liu, Projection method I: Convergence and numerical boundary layers, SIAM J. Numer. Anal. (1995) 1017–1057.
[44] V. Fadeev, I. Kvabtskhava, N. Komarov, Self-focusing of local plasma currents, Nucl. Fusion 5 (3) (1965) 202.
[45] D.A. Knoll, L. Chacón, Coalescence of magnetic islands, sloshing, and the pressure problem, Phys. Plasmas 13 (3) (2006) 32307–32311.
[46] J.H. Adler, M. Brezina, T.A. Manteuffel, S.F. Mccormick, J.W. Ruge, L. Tang, Island coalescence using parallel first-order system least-system least squares on incompressible resistive magnetohydrodynamics, SIAM J. Sci. Comput. 35 (5) (2013) S171–S191.
[47] J.N. Shadid, R.P. Pawlowski, J.W. Banks, L. Chacón, P.T. Lin, R.S. Tuminaro, Towards a scalable fully-implicit fully-coupled resistive MHD formulation with stabilized FE methods, J. Comput. Phys. 229 (20) (2010) 7649–7671.
[48] G.-D. Zhang, C. Chen, Uniformly robust preconditioners for incompressible MHD system, J. Comput. Appl. Math. (2020) 112914.
[49] E.C. Cyr, J.N. Shadid, R.S. Tuminaro, R.P. Pawlowski, L. Chacón, A new approximate block factorization preconditioner for two-dimensional incompressible (reduced) resistive MHD, SIAM J. Sci. Comput. 35 (3) (2013) B701–B730.
[50] S.R. Choudhury, The initial-value problem for the Kevin-Helmholtz instability of high velocity and magnetized shear layers, Qual. Appl. Math. LIV (1996) 637–662.
[51] T.W. Jones, J.B. Gaalaas, D.R.A. Frank, The MHD Kelvin-Helmholtz instability. II. The roles of weak and oblique fields in planar flows, Astrophys. J. (1997) 230–244.
[52] H. Baty, R. Keppens, P. Comte, The two-dimensional magnetohydrodynamic Kelvin-Helmholtz instability: compressibility and large-scale coalescence effects, Phys. Plasmas 10 (2003) 4661–4674.
[53] R. Hiptmair, L. Li, S. Mao, W. Zheng, A fully divergence-free finite element method for magnetohydrodynamic equations, Math. Models Methods Appl. Sci. 28 (04) (2018) 659–695.
[54] L. Li, W. Zheng, A robust solver for the finite element approximation of stationary incompressible MHD equations in 3D, J. Comput. Phys. 351 (2017) 254–270.